87Sr Solid-State NMR as a Structurally Sensitive Tool for the Investigation of Materials: Antiosteoporotic Pharmaceuticals and Bioactive Glasses

Christian Bonhomme,*,[†] Christel Gervais,[†] Nicolas Folliet,[†] Frédérique Pourpoint,[†] Cristina Coelho Diogo,[‡] Jonathan Lao,[§] Edouard Jallot,[§] Joséphine Lacroix,[§] Jean-Marie Nedelec,[⊥,¶] Dinu Iuga,[□] John V. Hanna,[□] Mark E. Smith,[□,▽] Ye Xiang,[#] Jincheng Du,[#] and Danielle Laurencin[$]

[†]Laboratoire Chimie de la Matière Condensée de Paris, UMR CNRS 7574, UPMC Université Paris 06, Collège de France, 11 place Marcelin Berthelot, 75231 Paris Cedex 05, France

[‡]IMPC, Institut des Matériaux de Paris Centre, FR2482, UPMC Université Paris 06, Collège de France, 11 place Marcelin Berthelot, 75231 Paris Cedex 05, France

[§]Clermont Université, Université Blaise Pascal, CNRS/IN2P3, Laboratoire de Physique Corpusculaire, BP 10448, 63000 Clermont-Ferrand, France

[⊥]Clermont Université, ENSCCF, ICCF, BP 10448, F-63000 Clermont-Ferrand, France

[¶]CNRS, UMR 6296, ICCF, F-63177 Aubière

[□]Department of Physics, University of Warwick, CV4 7AL Coventry, U.K.

[▽]Vice-Chancellor's Office, University House, Lancaster University, LA1 4YW, Lancaster, U.K.

[#]Department of Materials Science and Engineering, CASCaM, University of North Texas, Denton, Texas 76203, United States

[$]Institut Charles Gerhardt de Montpellier, UMR 5253, CNRS UM2 UM1 ENSCM, CC 1701 Université de Montpellier 2, Place E. Bataillon, 34095 Montpellier cedex 5, France

S *Supporting Information*

ABSTRACT: Strontium is an element of fundamental importance in biomedical science. Indeed, it has been demonstrated that Sr^{2+} ions can promote bone growth and inhibit bone resorption. Thus, the oral administration of Sr-containing medications has been used clinically to prevent osteoporosis, and Sr-containing biomaterials have been developed for implant and tissue engineering applications. The bioavailability of strontium metal cations in the body and their kinetics of release from materials will depend on their local environment. It is thus crucial to be able to characterize, in detail, strontium environments in disordered phases such as bioactive glasses, to understand their structure and rationalize their

properties. In this paper, we demonstrate that 87Sr NMR spectroscopy can serve as a valuable tool of investigation. First, the implementation of high-sensitivity 87Sr solid-state NMR experiments is presented using 87Sr-labeled strontium malonate (with DFS (double field sweep), QCPMG (quadrupolar Carr−Purcell−Meiboom−Gill), and WURST (wideband, uniform rate, and smooth truncation) excitation). Then, it is shown that GIPAW DFT (gauge including projector augmented wave density functional theory) calculations can accurately compute 87Sr NMR parameters. Last and most importantly, 87Sr NMR is used for the study of a (Ca,Sr)-silicate bioactive glass of limited Sr content (only ∼9 wt %). The spectrum is interpreted using structural models of the glass, which are generated through molecular dynamics (MD) simulations and relaxed by DFT, before performing GIPAW calculations of 87Sr NMR parameters. Finally, changes in the 87Sr NMR spectrum after immersion of the glass in simulated body fluid (SBF) are reported and discussed.
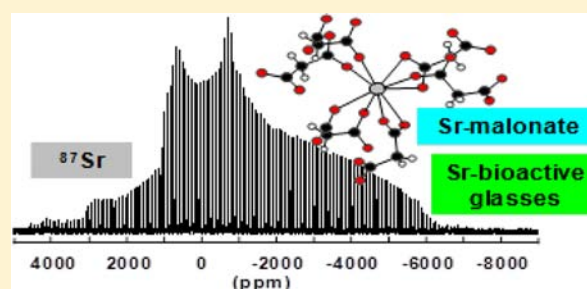
INTRODUCTION

The aging of the population is one of the main causes for the growing incidence of musculoskeletal problems and diseases, which call for the development of treatments for osteoporosis and of highly compatible and reliable bone substitutes. In this context, strontium is an element which is finding increasing interest, because it is now clearly established that strontium is

beneficial in bone remodeling. Strontium is a naturally occurring trace element, and as a bone seeker (like calcium), ∼99% of strontium present in the body accumulates in bone.[1,2] The absorption of pharmacological doses of strontium has been

associated with strengthening of bone, with the stimulation of bone formation and the decrease in bone resorption, and without affecting adversely bone mineralization.[3,4] Large randomized studies demonstrated that strontium supplements such as strontium ranelate (Protelos, Servier Laboratories, France) or strontium malonate (NB S101, Osteologix) decrease the risk of vertebral and nonvertebral fractures in women affected by postmenopausal osteoporosis, showing promise for strontium as a therapeutic agent in the treatment of osteoporosis.[3,5,6] Marked stimulatory effects of strontium ions on bone cells have also been evidenced, with enhanced osteoblast differentiation and alkaline phosphatase activity.[7−10]

The incorporation of strontium into bioactive biomaterials used for bone substitution, such as bioactive glasses, aims at the release of the biologically active Sr^{2+} ions directly at the site of implantation, while maintaining the inherent performance of the bioactive glasses in terms of bone regeneration. During the last five years, there has been a gradual increase in the number of scientific publications and patents concerning Sr-containing bioactive glasses. Recently, Jallot et al.[11] and Hill et al.[12] patented different series of strontium-containing glass compositions for bone regeneration, and the glasses based on Hill's patent are currently commercialized as StronBone by RepRegen Ltd. In calcium-silicate bioactive glasses, it is quite easy to incorporate Sr by replacing Ca ions in the initial glassy matrix, both being alkaline earth elements. However, it is not clear how substituting Sr for Ca in the glassy matrix affects the overall *glass structure*, the silicate network, and its polymerization. In addition, several discrepancies have been observed in the literature regarding the structure−property relationships of such bioactive glasses. The precise role of Sr^{2+} in the *glass chemistry* is thus not well understood and still debated, despite the fact that it is of major concern, affecting the thermal behavior, glass dissolution, release of ionic products, and bioactivity of the material. For example, the apatite-forming ability of sol−gel-derived glasses from the $SiO_2-CaO-SrO$ and $SiO_2-CaO-SrO-P_2O_5$ phase diagrams was first studied by Lao et al.,[13,14] who clearly provided evidence of reduced dissolution in the presence of Sr, and of the growth of the newly formed phosphocalcic surface layer. O'Donnell and Hill[15] hypothesized that this was due to the Sr^{2+}/Ca^{2+} ratio in the glass composition that varied on a weight basis, which would necessarily result in an increase in the silica content (on molar basis), thus leading to an increase in the network connectivity of the glass and to a subsequent slower dissolution and decreased bioactivity. This simple explanation is however refuted by the results obtained by Hesaraki et al.,[9] who varied the Sr^{2+}/Ca^{2+} ratio on a molar basis, with the Sr-glasses still exhibiting a significant delay in the formation of the apatite surface layer. The comparison from one author to another is all the more difficult, as a wide range of glass compositions has been studied so far (e.g., with or without Na_2O, P_2O_5, CaF_2, etc.), and that, above all, two completely different synthesis routes exist to produce bioactive glasses, namely the classic quenching of melts[15−18] and the sol−gel process.[9,13,14] Hill et al.[15] admit that the glass network connectivity cannot be calculated the same way, as it depends on the synthesis route: in particular, their estimation of the network connectivity cannot be applied to sol−gel-derived glasses. It is likely that the role of Sr in the glassy matrix also significantly differs depending on the synthesis route. Indeed, recently, Taherkani et al.[19] studied $SiO_2-CaO-SrO-P_2O_5$ sol−gel glasses where the SrO content varied between 0 and 36 mol %: they showed

the presence of unexpected rodlike crystal fibers at the surface of glasses with a high Sr content, before their stabilization at 700 °C. On the contrary, several studies on melt-quenched Sr-containing glasses showed that increasing the Sr/Ca ratio in the glasses did not affect their structure significantly,[17,20−22] although their apatite-forming ability is considerably decreased. It is not obvious then that Sr^{2+} assumes the same role as Ca^{2+} in sol−gel-derived glasses. This perspective would be of huge interest because it could be used as an additional means for designing glasses with tailored dissolution and ion release kinetics. An attempt to understand the structural role of Sr in bioactive glasses was recently performed by Du et al. through extensive molecular dynamics (MD) simulations of Sr-substituted bioactive glasses,[23] which showed that Sr and Ca may have different coordination numbers within the glass matrix. However, until now, there has been no precise *experimental* evidence of Sr local environments, and although a large multiscale suite of characterization techniques has already been used, including FTIR, XRD, thermal analysis, ^{29}Si and ^{31}P MAS NMR, SEM-EDS, and ion beam analyses, the question of the influence of Sr^{2+} on the structure and dissolution kinetics of glasses remains largely uncertain. A better understanding of the precise role of Sr in bioactive glasses calls for the development of an advanced dedicated Sr-sensitive technique to probe directly the local environment of Sr^{2+} ions.

Several questions also remain concerning the incorporation of strontium ions into the bioactive bonelike phosphocalcic *surface* layer that is mineralized when glasses are put in contact with a biological medium. Bone mineral is indeed dominated by a poorly crystalline fraction of substituted hydroxyapatite and other calcium phosphate compounds.[24] As such, Sr^{2+} can be incorporated into the newly formed bioactive apatitic layer either by substitution inside the apatite crystal lattice of bone or nonspecifically by ionic exchange with surface Ca^{2+} ions.[25,26] The latter would provide relatively quick uptake into new bone and possibly a quick release of the osteoinductive Sr^{2+} ions toward the bone cells. Clearly, the influence of Sr on the bioactivity of glasses concerns not only possible changes in the glass structure and chemistry but is also related to the bioavailability of the Sr^{2+} ions during the mineralization process. The fate of Sr in these bioactive glasses is not addressable by classic diffraction techniques, because of the poor crystallinity and limited domain size of the new phases which form in the early stages after immersion of the glass in physiological fluid. Characterization techniques sensitive to Sr local environments are thus also needed to understand better the structural changes in the material under physiological conditions.

Very few spectroscopic techniques are available to characterize Sr local environments, because Sr^{2+} is a closed shell diamagnetic cation. Indeed, although X-ray diffraction (XRD) can provide information on the coordination environment of strontium,[27] this technique cannot be used for the study of a large number of strontium compounds, because they do not form crystals suitable for XRD or because they are available only in disordered or amorphous forms, as is the case for Sr-containing bioactive glasses. For such materials, other experimentally challenging techniques are available, such as Sr K-edge X-ray absorption spectroscopy and ^{87}Sr solid-state NMR, both of which require specific facilities (i.e., a synchrotron beamline or a high field NMR magnet). Only a few Sr K-edge X-ray absorption spectroscopy studies have been

reported on manufactured or natural materials.[28−33] These have shown that distances between Sr and its nearest neighbors can be determined and that averaged information on the number of neighbors in the different coordination spheres can be accessed. However, to the best of our knowledge, such characterization approaches have not yet been carried out on Sr-containing bioactive glasses. On the other hand, a small number of ^{87}Sr solid-state NMR experiments have been published,[34−39] showing that ^{87}Sr quadrupolar NMR parameters (i.e., the quadrupolar coupling constant C_Q and the asymmetry parameter η_Q) are sensitive to Sr local environments, and may thus provide information on the local structure around Sr in complex materials. Nevertheless, the number of ^{87}Sr solid-state NMR experiments reported so far has also remained very limited, because strontium-87, the NMR active isotope, is a spin 9/2 low-gamma (i.e., with a small magnetic moment) nucleus of low natural abundance (7%) with a large quadrupole moment.[40] The significant quadrupolar interaction usually experienced produces very broad lineshapes, and most ^{87}Sr NMR experiments have thus been recorded in "static" mode to be able to extract accurate ^{87}Sr NMR parameters using pulse sequences such as QCPMG (quadrupolar Carr−Purcell−Meiboom−Gill)[41] and signal enhancement schemes such as DFS (double frequency sweep).[42] Despite the promising first developments of ^{87}Sr solid-state NMR, this technique has never been applied to the characterization of Sr-containing bioactive materials. As a matter of fact, ^{87}Sr solid-state NMR has remained largely unexplored since 2006, meaning that more recent NMR pulse sequences such as WURST (wideband uniform rate smooth truncation), which have proven their efficiency for the characterization of other quadrupolar nuclei with large quadrupole moments,[43−48] have not yet been tested for strontium-87. Furthermore, the possibility of using first principles DFT (density functional theory) calculations based on the GIPAW (gauge including projector augmented wave) method[49] to calculate NMR parameters, thereby assisting the implementation of NMR experiments and in the interpretation of the NMR data, has not yet been investigated for strontium-87, despite the increasing use of this methodology in materials science.[50]

The purpose of this article is to try to shed light on the local environment of Sr in sol−gel-prepared bioactive glasses before *and* after immersion in physiological fluids, using ^{87}Sr solid-state NMR in a combined experimental−computational approach. To study the sole influence of Sr on the glass characteristics, we felt it more appropriate here to study a simple composition based on a SiO$_2$−CaO−SrO phase. Indeed, the risk of multiple interfering parameters becomes high when studying more complex compositions (with for example P$_2$O$_5$ or Na$_2$O). Moreover, this composition has already been proved to be bioactive,[7,13] and the effect of Sr in reducing the glass dissolution rate is even more pronounced than with glasses of more complex composition.[14] The glass composition chosen here was 75.0SiO$_2$−15.0CaO−10.0SrO (wt %) (glass referred to as B75-Sr10 in this manuscript).[51] It should be noted that the SrO content chosen for B75-Sr10 did not exceed 10 wt % for the glass to be capable of releasing physiological concentrations of Sr^{2+} ions, inducing a beneficial osteoinductive effect on bone cells.

Before characterization of the B75-Sr10 bioactive glass, several new developments in ^{87}Sr solid-state NMR spectroscopy were performed, which will be presented in the first part of this article. First, the DFS−WURST−QCPMG variable offset cumulative spectroscopy (VOCS) ^{87}Sr NMR experiment was implemented and optimized using an ^{87}Sr-enriched crystalline Sr-malonate sample and then extended at natural abundance to several other crystalline phases (Sr-phosphates, Sr-silicates, Sr-phenylphosphonate, Sr-phenylboronate), to increase the experimental data available. On the basis of all these new experimental data, GIPAW was then demonstrated to be a suitable approach for the accurate calculations of ^{87}Sr NMR quadrupolar parameters, meaning that GIPAW calculations can be used for assigning spectra in the case of multiple site structures. On the basis of this new methodology, the ^{87}Sr NMR spectrum of the B75-Sr10 bioactive glass (synthesized as an ^{87}Sr-enriched phase) was recorded at 20 T. To help interpret the complex lineshape, extensive computational modeling of the glass was performed (combining molecular dynamics (MD), first principles DFT), followed by GIPAW calculations on these models. Finally, the ^{87}Sr NMR spectrum of B75-Sr10 bioactive glass after immersion in SBF (simulated body fluid) was also recorded, showing that information on the evolution of the local structure around Sr upon immersion of bioactive glasses can be accessed.

■ MATERIALS AND METHODS

Syntheses. High purity malonic, phenylboronic, and phenylphosphonic acid reagents and SrCl$_2$·6H$_2$O were purchased from Acros, Alfa Aesar, and Aldrich, and used as received. Enriched *SrCO$_3$ (with 90% Strontium-87) was purchased from CortecNet. Commercial tetraethylorthosilicate (TEOS, Si(OC$_2$H$_5$)$_4$), calcium nitrate tetrahydrate (Ca(NO$_3$)$_2$,4H$_2$O), Sr(NO$_3$)$_2$, Na$_2$SiO$_3$·5H$_2$O, and D$_2$O were used as received. Reagent grade solvents were used in all reactions, as well as purified water. SrS, SrB$_6$, SrCO$_3$, Sr(NO$_3$)$_2$, and SrHPO$_4$ were purchased from Aldrich and analyzed by ^{87}Sr NMR as received.

Sr-phenylboronate (Sr(C$_6$H$_5$B(OH)$_3$)$_2$·H$_2$O)[52] and α-SrP$_2$O$_6$[53] were synthesized according to published procedures. The syntheses of Sr-phenylphosphonate (Sr(C$_6$H$_5$PO$_2$(OH))$_2$) and deuterated Sr-phenylboronate (Sr(C$_6$H$_5$B(OD)$_3$)$_2$·D$_2$O) can be found in the Supporting Information, while the syntheses of Sr-malonate, SrSiO$_3$, Sr$_3$(PO$_4$)$_2$, and the B75-Sr10 bioactive glass are given below. The coordination environments of the Sr atoms in SrCO$_3$, Sr(NO$_3$)$_2$, Sr-malonate, Sr-phenylboronate, Sr-phenylphosphonate, α-SrP$_2$O$_6$, Sr$_3$(PO$_4$)$_2$, and SrSiO$_3$ are shown in Figure S1 (from hereon, "S" refers to the data in Supporting Information). Representative powder XRD patterns of some crystalline samples (both commercial and synthetic) are presented in Figure S2 (Supporting Information).

*^{87}Sr-Labeled Sr-malonate (anhydrous), *Sr(CH$_2$(COO))$_2$.* First, 120 mg of enriched *SrCO$_3$ (0.81 mmol, 1 equiv) was placed in an alumina crucible and heated to 1000 °C under a stream of Ar to form *SrO. After 1 h of heating, the crucible was left to cool to room temperature. Then, 85 mg of malonic acid (0.81 mmol, 1 equiv) was dissolved in 2 mL of ultrapure water, and the *SrO solid was added progressively under stirring, leading to the dissolution of the solid. After a few minutes, a white solid precipitates in the medium. The suspension was stirred for ∼12 h at room temperature, after which it was centrifuged. The supernatant was removed and the white solid dried twice with diethylether and then further dried at 40 °C (100 mg, yield: 65%). The synthesis was repeated twice to ensure that enough product would be available for the ^{87}Sr NMR experiments. It is noteworthy that attempts to prepare the *hydrated* form of Sr-malonate following a procedure described in the literature[27] were unsuccessful, as they systematically led to the dehydrated salt. IR (for the nonenriched sample prepared following the same synthetic procedure) (KBr, cm$^{−1}$): 3009 (w), 2914 (w), 1587 (s), 1406 (m), 1356 (s), 1175 (w), 988 (w), 982 (w), 952 (w), 944 (w), 828 (w), 701 (m), 664 (m), 574 (m), 464 (w).

*^{87}Sr-Labeled *Sr$_{10}$(PO$_4$)$_6$(OH)$_2$ (belovite), *SrHPO$_4$, and *Sr$_3$(PO$_4$)$_2$.* First, 117 mg (∼0.8 mmol) of *SrCO$_3$ was heated to 1000 °C for 8 h, under a stream of Ar, leading to the formation of ∼83

mg of *SrO (~0.8 mmol). This white powder was then suspended in 1.5 mL of ultrapure H_2O, and the mixture was heated to 90 °C under an Ar atmosphere. An aqueous solution of H_3PO_4 was then added drop by drop (0.45 mL of a 1 mol·L^{-1} solution) under stirring. The suspension was stirred for ~24 h at 90 °C (under Ar). At this stage, 0.05 mL of an aqueous solution of NH_4OH (1 mol·L^{-1} concentration) was added to the suspension. The stirring was then continued for a further ~16 h at 90 °C (under Ar). After return to room temperature, the suspension was centrifuged, and the resulting white powder was washed three times with ultrapure H_2O, before being dried under vacuum at 100 °C for 14 h. The XRD powder pattern of this sample reveals that it is a mixture of *$SrHPO_4$ and *$Sr_{10}(PO_4)_6(OH)_2$ (belovite). After ^{87}Sr NMR experiments, this sample (~80 mg) was thus further heat treated at 1050 °C for 3 h, under a stream of Ar. The resulting white powder (~68 mg) was identified by XRD as pure *$Sr_3(PO_4)_2$ (see Figure S2).

SrSiO₃. A 0.5 M $Sr(NO_3)_2$ solution was added drop by drop into a 0.5 M Na_2SiO_3 solution at room temperature for 12 h. The precipitate was then washed sequentially in distilled water and anhydrous ethanol, dried at 60 °C for 24 h, and finally calcined at 900 °C for 2 h. The final calcination step was repeated after intermediate grinding. The XRD powder pattern of the final product (Figure S2) confirms its purity, by comparison with the reference pattern of $SrSiO_3$ (ICSD 59308).

B75-Sr10 Bioactive Glass.[51] Glasses in the SiO_2–CaO–SrO phase diagram were synthesized using the sol−gel process.[14,54] The targeted glass composition of the glass named B75-Sr10 was 75.0SiO_2–15.0CaO–10.0SrO (wt %) (or 77.4SiO_2–16.6CaO–6.0SrO (mol %)). It was prepared by mixing 13.94 mL of TEOS, 3.158 g of $Ca(NO_3)_2$·4H_2O, and 1.021 g strontium nitrate $Sr(NO_3)_2$ in ethanol in the presence of deionized water and 2 N HCl under ambient pressure and temperature. The quantities of reactants were calculated using a H_2O:TEOS molar ratio of 12:1 and a H_2O:HCl volume ratio of 6:1. A 50 mL low viscosity sol was obtained and stirred for 1 h. The prepared sol was then transferred to airtight PTFE molds in an oven at 60 °C for gel formation and aging. After 24 h, the obtained gels were heated at 125 °C for another 24 h, ground to powder, and then stabilized at 700 °C to eliminate nitrate and further densification. Chemical analyses by ICP-AES (found): 74.9SiO_2–16.0CaO–9.1SrO (wt %) (or 76.9SiO_2–17.6CaO–5.5SrO (mol %)).

*^{87}Sr-Labeled Bioactive Glass. B75-*Sr10.* ^{87}Sr-enriched glasses in the SiO_2–CaO–SrO phase diagram were also synthesized using the sol−gel process, with the same targeted composition as for B75-Sr10. In this case, *$SrCO_3$ was first mixed in water in the presence of 2 N HCl. After complete dissolution of the strontium carbonate, EtOH, deionized water, TEOS, and calcium nitrate were added, following the protocol described above. Two labeled samples (~500 mg each) were synthesized for further ^{87}Sr NMR characterization and reaction with simulated body fluid, SBF (see below). The experimental compositions of both samples were determined using ICP-AES. First sample (found): 77.4SiO_2–14.9CaO–7.7SrO (wt %) (or 79.1SiO_2–16.3CaO–4.6SrO (mol %)). Second sample (found): 75.5SiO_2–15.3CaO–9.2SrO (wt %) (or 77.6SiO_2–16.9CaO–5.5SrO (mol %)). In vitro tests with SBF were carried using the second sample, as its composition is closer to the nominal one.

In Vitro Interaction of the Bioactive Glass Grains with SBF and Deuterated SBF. ^{87}Sr labeled B75-*Sr10 glasses were left to interact in vitro within an acellular medium (SBF) for 7 days. The ionic composition of SBF is close to human blood plasma; it is commonly used to simulate the interaction with a biological environment and to induce mineralization. SBF was prepared following the procedure initially proposed by Kokubo et al.[55] for c-SBF ("corrected-SBF") and recently improved by Bohner et al. (for corresponding c-SBF2).[56] In addition, deuterated-SBF (referred to herein as d-SBF or SBF-D_2O) was prepared in view of enhanced detection of ^{87}Sr in the NMR characterization of the mineralized layer at the B75-*Sr10 glass surface (see below). The synthesis of d-SBF was the same as for conventional SBF except for the use of deuterated water D_2O instead of H_2O. Then, 20 mg of glass grains was immersed in 20 mL of SBF or d-SBF for 7 days at a constant ratio of 1 mg biomaterial per mL of fluid.[57] This procedure was replicated 25 times to ensure reproducibility; thus, a

total amount of 500 mg of B75-*Sr10 was tested in vitro for the two acellular media (SBF and d-SBF). After 7 days of interaction with biological fluids, the glass grains were removed from the fluids, rinsed with acetone, and finally air-dried at room temperature.

Chemical analyses (ICP-AES) on the glass grains after 7 days interaction (found): B75-*Sr10-d-SBF: 77.8SiO_2–15.3CaO–1.8SrO–4.8P_2O_5–0.3MgO (wt %). B75-*Sr10-SBF: 76.6SiO_2–15.8CaO–1.7SrO–5.7P_2O_5–0.2MgO (wt %). It follows from these chemical analyses that ~80.5% of the initial Sr content in the bioactive glass has been released in the SBF medium. The supernatant SBF and d-SBF solutions were analyzed as well (after immersion) by ICP-AES (titration of P, Mg, Si, Ca, and Sr elements). On average, the solution titrations confirm that ~78% of the initial Sr content in the bioactive glass has been released in the SBF medium, which is thus in fair agreement with the data obtained from the chemical analyses of the powders recovered after immersion.

It is important to stress here that the compositions of all glasses studied are very rich in the silica phase in contrast to the Ca/Si glasses already reported in the literature and studied by NMR.[58,59]

Solid-State NMR. ^{87}Sr NMR experiments were performed at high magnetic field (600 MHz AVANCE II$^+$ and 700 MHz AVANCE III Bruker spectrometers) and ultrahigh magnetic field (850 MHz AVANCE III Bruker spectrometer) using low-gamma 3.2, 4, 5, and 7 mm Bruker probes, and a 9.5 mm Varian probe (coupled to a low-gamma box). Both magic angle spinning (MAS) and static experiments were performed. Details on which probes were used are given in the figure captions. SrS and SrB₆ (cubic structures) were studied by single pulse excitation (SPE) MAS NMR experiments. All other samples were characterized by *static* ^{87}Sr NMR, because of their much larger quadrupolar constants. Indeed, broad patterns under MAS are expected, but with no possibility to separate the spinning sidebands from the isotropic centerbands, creating difficulties in the extraction of the quadrupolar parameters. The static experiments used were a combination of DFS−WURST−QCPMG[43,60,61] and VOCS experiments.[62,63] To enhance the population of the central transition, typically a 6 kHz RF field strength convergence sweep from 800 kHz to 200 kHz (duration: 1 ms) was used in the DFS.[42] The setup was adapted taking into account the reflected power from the probes. WURST-80 pulse shapes with a 45 μs WURST pulse length, swept at a rate of 22 MHz/ms, with a sweep width of 1000 kHz and typical RF power of 7 kHz, were used. All experimental parameters were adapted to each individual sample, with the number of VOCS offsets chosen according to the line widths (which are broadened by different second-order quadrupolar effects). GIPAW calculations were used as an initial estimate of the C_Q values (see below).

To determine the effect of ^1H decoupling during ^{87}Sr DFS−WURST−QCPMG acquisition, a low-gamma 7 mm H-X DOTY probe was used (600 MHz AVANCE II$^+$) with 15 kHz power ^1H decoupling (continuous wave decoupling, CW). The decoupling power was deliberately limited, as long acquisition times (up to 100 ms) are employed in the DFS−WURST−QCPMG experiments. Sr-malonate and Sr-phenylboronate were used as test samples. A partly deuterated Sr-phenylboronate sample ($Sr(C_6H_5B(OD)_3)_2$·D_2O) was also studied to further estimate the impact of ^1H−^{87}Sr dipolar couplings on the ^{87}Sr NMR spectra.[48,64]

All ^{87}Sr NMR spectra were referenced against a 1.0 M aqueous solution of $SrCl_2$ (0.0 ppm, relaxation delay: 0.1 s). A 0.1 M aqueous solution of $SrCl_2$ led to a signal at −0.8 ppm. For each ^{87}Sr NMR spectrum, the full details, including relaxation delays, total experimental times, and number of offsets, are given in the figure captions. The simulations of the NMR spectra were performed using the DMFit[65] and QUADFIT[66] numerical platforms.

Modeling of Glasses. Strontium-containing glasses including, binary SiO_2–SrO, ternary SiO_2–CaO–SrO, and more complex SiO_2–Na_2O–CaO–SrO–P_2O_5 phases were simulated using MD. The glass compositions chosen were 76.9SiO_2–17.6CaO–5.4SrO (mol %), 93.4SiO_2–6.6SrO (mol %) and 46.1SiO_2–24.4Na_2O–16.9CaO–10.0SrO–2.6P_2O_5 (mol %), respectively. The first composition corresponds approximately to the nominal one of B75-Sr10. The second one corresponds to the same Sr/Si ratio but Sr atoms are part

Table 1. Experimental and Calculated (PWSCF) GIPAW Data for Sr Compounds after Relaxation of H Positions When Needed[a]

	ICSD			δ_{iso}	Δ_{CSA}	η_{CSA}	C_Q	η_Q
SrO	109461	PWSCF	#1	340.0	0.0	–	0.00	0.00
		exp	#1	340.0[b]				
SrB₆	50313	PWSCF	#1	100.0	0.0	–	0.00	0.00
		exp	#1	~ 100[c]			c	c
SrCO₃	202793	PWSCF	#1	−35.8	−52.3	0.13	8.49	0.55
		exp	#1	0 ± 20			8.91[b]	0.14[b]
Sr(NO₃)₂	59391	PWSCF	#1	−151.4	−9.4	0.00	−18.41	0.00
		exp	#1	−70 ± 30			15.30[b]	0.03[b]
Sr-malonate	IUCr A14762	PWSCF	#1	−65.5	51.0	0.78	−34.91	0.91
		exp	#1	0 ± 60			31.5	0.80
Sr-phenylboronate	CCDC 816692	PWSCF	#1	−3.9	62.3	0.89	−21.15	0.90
		exp	#1	50 ± 60			20.2	0.25
Sr-phenylphosphonate	CCDC 271466	PWSCF	#1	−50.4	−12.1	0.93	−35.73	0.41
		exp	#1	0 ± 200			34.5	0.65
α-SrP₂O₆	415334	PWSCF	#1	−43.9	55.2	0.24	32.91	0.12
			#2	−46.7	56.5	0.88	35.45	0.62
			#3	−62.7	64.2	0.50	40.72	0.31
			#4	−46.7	54.5	0.43	35.57	0.08
		relax	#1	−45.7	45.7	0.47	33.91	0.23
			#2	−46.6	49.9	0.77	37.26	0.41
			#3	−55.5	53.5	0.17	36.76	0.15
			#4	−43.5	45.4	0.64	33.98	0.17
		exp		d			d	d
β-SrP₂O₆	402461	PWSCF	#1	−14.4	31.9	0.62	42.53	0.55
			#2	−50.2	50.8	0.58	45.60	0.29
		relax	#1	−15.5	37.6	0.71	40.86	0.72
			#2	−51.2	57.0	0.37	48.64	0.17
α-Sr₂P₂O₇	59395	PWSCF	#1	−91.1	−28.1	0.62	−21.99	0.01
			#2	−21.5	84.8	0.60	−40.27	0.49
		relax	#1	−76.3	−35.3	0.47	−24.82	0.19
			#2	−0.1	97.6	0.47	−38.86	0.86
SrHPO₄	91129	PWSCF	#1	−76.9	−91.2	0.21	−51.16	0.55
			#2	−35.6	−26.1	0.75	12.90	0.71
belovite Sr₁₀(PO₄)₆(OH)₂	2855	PWSCF	#1	17.9	−78.7	0.00	−52.13	0.00
			#2	41.3	−99.8	0.79	−25.30	0.51
SrSiO₃[e]	59308	PWSCF	#1	19.9	65.9	1.00	16.80	0.66
			#2	20.3	−158.0	0.18	−40.90	0.81
		relax	#1	26.8	69.9	1.00	19.35	0.54
			#2	24.8	−167.4	0.17	−42.60	0.71
		exp	#1	0 ± 70			18.5	0.45
			#2	0 ± 100			46.0	0.4
Sr₃(PO₄)₂	150869	PWCSF	#1	−25.2	−49.2	0.00	−59.97	0.00
			#2	−18.4	−74.2	0.00	−22.67	0.00
		relax	#1	0.8	−53.2	0.00	−63.41	0.00
			#2	−34.6	−92.6	0.00	−30.48	0.00
		exp	#1	0 ± 200			69.0	0.1
			#2	0 ± 100			30.5	0.1
Sr₃SiO₅[e]	418933	PWCSF	#1	218.6	−64.8	0.04	−34.66	0.57
			#2	156.7	−162.4	0.00	−26.01	0.00
CaSrSiO₄[e]	20544	PWCSF	#1	91.2	−114.6	0.52	−35.63	0.83
			#2	119.3	−115.5	0.87	−52.24	0.92
			#3	109.0	100.8	0.82	−49.04	0.77

[a]In the case of nonprotonated structures, "relax" means that *all* atomic positions in the initial structure have been relaxed under DFT, as detailed in Materials and Methods. δ_{iso} is in ppm (referenced to aqueous SrCl₂, 1 M), and C_Q in MHz. # indicates the site number in the crystallographic structure (for the PWSCF calibration with SrO and SrB₆, see Figure S3a). CASTEP calculations are given in Table S2 (including those for SrS, SrSO₄, SrF₂, and SrCl₂). The definitions of Δ_{CSA} and η_{CSA} are given in Materials and Methods. [b]See refs 37 and 39. [c]For SrB₆, two components at δ_{iso} ~ 100 ppm were observed (C_Q = 0.7 MHz and C_Q = 5.1 MHz; see Figures S14 and S15). [d]See text and Figure S17 for α-SrP₂O₆. [e]GIPAW-computed δ_{iso}(^{29}Si): SrSiO₃ (Q^2 units): −83.9 and −84.0 ppm; Sr₃SiO₅ (Q^0 units): −68.8 ppm; CaSrSiO₄ (Q^0 units): −68.1, −68.0, −73.9 ppm.

of a pure silica-like phase. The third one is derived from the 45S5 Bioglass ($46.1SiO_2-24.4Na_2O-26.9CaO-2.6P_2O_5$ (mol %)), which was first proposed by Hench and is generally considered as the standard reference in the field.[67] The glass compositions, densities, and cell information are listed in Table S1. Systems of ~200 atoms were chosen to make the next step (first principles DFT relaxation) and further NMR calculations possible using currently available computational resources. For each composition, five independent glasses starting from different randomly generated initial structures were prepared to provide statistics of the structures, especially of the local environments of Sr in these glasses. The force field employed in this series of MD simulations uses partial charge pairwise potentials with the Buckingham form. These potentials have already been used to model Sr-glasses exhibiting large simulation cells with several thousands of atoms, and favorable comparison with experimental structural data (density + neutron diffraction data) had been obtained.[23,68] The effectiveness and transferability of such potentials in simulating alkali silicate and phosphosilicate glasses have also been proved in various studies of multicomponent glass systems.[69,70] MD simulations were carried out using the DL-POLY code 2.20 developed by Smith and Forester.[71] To maintain the simulated glass density equal to the experimental values, constant volume canonical (NVT) and microcanonical (NVE) ensembles were used in the glass simulation procedures. The initial configurations were generated with a random distribution of atoms with constraints of shortest distances between each atom pair in cubic simulation cells, with the atom numbers and cell dimensions consistent with the experimental composition and glass density. The Verlet Leapfrog algorithm was used to solve the integration of Newtonian equations with a time step of 1 fs (fs). The initial structure was relaxed at 0 K before the melt-and-quench glass formation process. The samples were melted by gradually increasing the temperature to ~6000 K, at which temperature the samples were run for 600 000 steps under NVT ensemble and another 600 000 steps under NVE ensemble. The system was then gradually cooled down by 500 K intervals, and the final temperature was 300 K. The simulations were performed for 600 000 steps at each temperature with a nominal cooling rate of 0.5 K/ps. Such a slow cooling rate employed in MD simulation was chosen to improve structural information of phosphorus-containing glasses, as discussed in an earlier study.[68] During the final steps at 300 K, configurations were collected every 100 steps in the last 400 000 steps of NVE run for final structure analysis. The five structure models of each glass composition obtained from MD simulations were then further optimized using first principles density functional theory (DFT) calculations with the Vienna Ab Initio Simulation Package (VASP).[72,73] The projector-augmented wave (PAW)[74,75] pseudopotentials and generalized gradient approximation (GGA) exchange and correlation functional with the PBE[76,77] parametrization were used in the calculations. The kinetic energy cutoff for plane waves was 400 eV and Brillouin zone sampling with meshes generated by the Monkhorst–Pack[78] scheme was used for the integration in reciprocal space. Gamma point sampling was used during the relaxation while $2 \times 2 \times 2$ sampling was used during the geometry optimization. All atom positions were fully relaxed until the forces acting on each of the atoms was smaller than 0.01 eV/Å. The fully relaxed structural models were used as input in NMR spectra calculations.

Computational Details of NMR Calculations. One of the two approaches applied here for NMR calculations within Kohn–Sham DFT consisted of using the free QUANTUM-ESPRESSO software (available online),[79] which is an integrated suite of computer codes including PWSCF (plane wave self-consistent field) for electronic structures calculations and GIPAW[49] for NMR parameter calculations. In a first step, the strontium pseudopotential was generated and optimized by comparing calculated and experimental ^{87}Sr NMR parameters of $SrCO_3$ and $SrNO_3$. Typically, the following parameters were adjusted: (i) the valence-core partition (either $5s^2$ or $4s^24p^65s^2$ for valence electrons); (ii) the type of pseudization (either Troullier Martins[80] or Rappe–Rabe–Kaxiras–Joannopoulos);[81] (iii) the type of pseudopotential (either norm-conserving[82] or ultrasoft);[83] (iv) the pseudization radii. Transferability was checked by testing the results of

pseudopotentials and all electron atomic calculations on atomic configurations differing from the starting ones (for instance $5s^0$). A total energy difference between pseudopotentials and all electron results lower than 10 mRy was considered acceptable. The PBE generalized gradient approximation[76] was used, and the valence electrons were described by norm-conserving pseudopotentials in the Kleinman–Bylander form. The core definition for B, C, N, and O was $1s^2$, $1s^22s^22p^6$ for Si and P and $1s^22s^22p^63s^23p^63d^{10}4s^24p^6$ for Sr. The core radii were 1.2 au for H, 1.2 au for B, 1.6 au for C, 1.5 au for O and N, 2.0 au for Si and P, and 3.7 au for Sr. The wave functions were expanded on a plane wave basis set with a kinetic energy cutoff of 80 Ry. The crystalline structure was described as an infinite periodic system using periodic boundary conditions. The NMR calculations were performed on the experimental geometries summarized in Table 1. In the case of Sr-malonate, Sr-phenylphosphonate, Sr-phenyl-boronate, $SrHPO_4$, and $Sr_{10}(PO_4)_6(OH)_2$, proton atomic positions were adjusted by relaxation of the atomic forces while the cell parameters were kept constant. For some nonprotonated derivatives, GIPAW calculations were performed for both fully relaxed and nonrelaxed structures (see Table 1 for details). PWSCF calculations were performed on the IDRIS supercomputer center of the French CNRS.

An alternative approach adopted here was to start from the structures described above (including proton relaxation) and to perform GIPAW calculations using the CASTEP program, which is still the most commonly used approach within the solid-state NMR community.[84] All CASTEP calculations were performed using dual-2.0 GHz/dual core Hewlett-Packard xw9300 AMD Opteron workstations and required no more than 4 GB of RAM. NMR CASTEP was run through the Accelrys Materials Studio Modeling 4.2 interface, using the GGA (PBE) functional. The unit cell and symmetry recommended by the interface were accepted. Prerelease B, C, N, S, O, and Sr on-the-fly pseudopotentials were provided by Accelrys Company. These are ultrasoft pseudopotentials which will allow a comparison with the norm-conserving ones optimized for the QUANTUM-ESPRESSO calculations. It should be noticed that the choice of the type of pseudopotential is independent of the code.

The isotropic chemical shift δ_{iso} is defined as $\delta_{iso} = -[\sigma - \sigma^{ref}]$ where σ is the isotropic shielding and where σ^{ref} was extracted for both types of calculations. For PWSCF calculations (QUANTUM-ESPRESSO), the correlation between calculated and experimental data is presented in Figure S3a for SrO and SrB_6. Both structures are cubic, and standard MAS experiments lead to accurate experimental measurements of $\delta_{iso}(^{87}Sr)_{exp}$ (see discussion below and ref 37). The slope of the linear correlation was fitted freely and allowed extraction of σ^{ref}. Data corresponding to other cubic structures such as SrS, SrF_2, and $SrCl_2$ were not considered here, as accurate pseudopotentials for S, F, and Cl were not available in QUANTUM-ESPRESSO (PWSCF). For CASTEP calculations, the correlation between calculated and experimental data is presented in Figure S3b for SrO, SrB_6, SrS, SrF_2, and $SrCl_2$; the slope of the linear correlation was fitted freely and allowed extraction of σ^{ref}. For both types of calculations, diagonalization of the symmetrical part of the calculated tensor then provides its principal components σ_{11}, σ_{22}, σ_{33} from which the chemical shift components δ_{11}, δ_{22}, δ_{33} can be calculated. δ_{11}, δ_{22}, and δ_{33} are defined such as $|\delta_{33} - \delta_{iso}| \geq |\delta_{11} - \delta_{iso}| \geq |\delta_{22} - \delta_{iso}|$, and $\delta_{iso} = \frac{1}{3}(\delta_{11} + \delta_{22} + \delta_{33})$. The CSA parameters are defined by $\Delta_{CSA} = \delta_{33} - \delta_{iso}$ and $\eta_{CSA} = |(\delta_{22} - \delta_{11})/\Delta_{CSA}|$. The principal components V_{xx}, V_{yy}, and V_{zz} of the electric field gradient (EFG) tensor defined as $|V_{zz}| \geq |V_{xx}| \geq |V_{yy}|$ are obtained by diagonalization of the tensor. The quadrupolar interaction can then be characterized by the quadrupolar coupling constant C_Q and the asymmetry parameter η_Q which are defined as: $C_Q = eQV_{zz}/\hbar$ and $\eta_Q = (V_{yy} - V_{xx})/V_{zz}$ (e is the proton charge, $\hbar$ Planck's constant, and Q the quadrupole moment of the considered nucleus). The experimental value of the quadrupole moment of ^{87}Sr ($Q = 30.5 \times 10^{-30}$ m^2) was used to calculate C_Q.[85] PWSCF and CASTEP calculated data are given in Tables 1 and S2, respectively.

■ RESULTS AND DISCUSSION

Development of ^{87}**Sr NMR Experiments and Calculations.** *High Sensitivity* ^{87}*Sr NMR Spectroscopy and Simulation of* ^{87}*Sr NMR Lineshapes.* A variety of crystalline Sr-samples of biomedical interest (Sr-malonate, α-SrP$_2$O$_6$, Sr$_3$(PO$_4$)$_2$, SrSiO$_3$) or of potential interest for the development of hybrid materials (Sr-phenylboronate and Sr-phenylphosphonate) was first studied by ^{87}Sr NMR, to (i) implement a new experimental methodology for recording ^{87}Sr NMR spectra using some of the latest developments in NMR pulse sequences for quadrupolar nuclei, and (ii) determine how ^{87}Sr NMR lineshapes can be interpreted and simulated. As described in Materials and Methods, anhydrous Sr-malonate, *Sr(CH$_2$(COO)$_2$), was prepared as a ^{87}Sr-labeled sample. Labeled strontianite (*SrCO$_3$) was used as the Sr precursor in the synthesis: it is commercially available and can be subsequently manipulated after transformation into *SrO. This synthetic approach is similar to the one reported previously for ^{43}Ca NMR spectroscopy, starting from labeled calcite (*CaCO$_3$).[86] The demonstration of facile ^{87}Sr enrichment starting from labeled strontianite is important, as it paves the way to the development and application of ^{87}Sr solid-state NMR spectroscopy. Indeed, due to labeling, the signal-to-noise (S/N) ratio is very high, and Sr-malonate was thus used for the set up of the ^{87}Sr DFS−WURST−QCPMG experiment at a given offset and to verify the WURST efficiency (as illustrated in Figure S4a). The DFS parameters were set, making sure that the frequency range swept by the DFS pulse does not affect the signal corresponding to the CT; this was verified for each sample. A gain in intensity of ~1.3 was observed with DFS (see Figure S4b).

The static ^{87}Sr NMR spectrum corresponding to the unique crystallographic Sr site of the Sr-malonate is presented in Figure 1a. It corresponds to a well-defined second-order quadrupolar static lineshape,[40] centered at δ_{iso} = 0 ± 60 ppm. From the high S/N ratio, C_Q and η_Q values are accurately determined: C_Q = 31.5 ± 0.5 MHz (see Figure 1b) and η_Q = 0.80 ± 0.05. Interestingly, not only is the central transition (CT) observed, but the partial excitation of the satellite transitions (STs)[40b] is also evident at the very ends of the spectrum, as recently observed by QCPMG NMR for another spin 9/2 isotope, ^{209}Bi.[87] In addition, by looking carefully at the CT lineshape, the intensity of the signal is slightly overestimated in the [−2000 ppm, −4000 ppm] region when compared to the simulated spectrum (which only takes into account the CT). This may be due to CSA effects, to the ST, or to T$_2$ anisotropy effects (see below). In Figure S5, the effects of CSA are taken into account in the simulations. It is shown that for moderate anisotropies, Δ_{CSA} < 500 ppm, the effects on the lineshapes are hardly discernible. Based on GIPAW calculations (see below), Δ_{CSA} values are expected to be small (<170 ppm) and thus cannot lead to distortions of the lineshapes such as those observed in Figure 1. In Figure S6, the simulations of the CT and CT + ST are presented, showing that the intensity of the spectrum increases in the [−2000 ppm, −4000 ppm] region in the CT + ST simulation, in agreement with the experiment. It follows that STs may be responsible for the slight distortion of the lineshape. However, QCPMG spectra can also show significant distortions due to T$_2$ anisotropy caused by dynamic effects. This particular phenomenon was observed by O'Dell et al.[48] in the case of ^{14}N NMR and could play also a role in the distortion observed here.
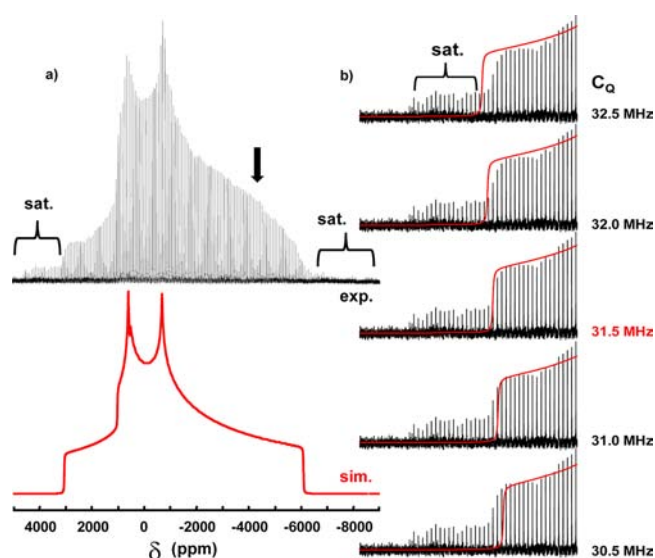
Figure 1. (a) Static DFS−WURST−QCPMG ^{87}Sr NMR spectrum of Sr-malonate, SrCH$_2$(COO)$_2$. Experimental parameters: 19.8 T, 7 mm low-gamma Bruker probe, static mode, DFS convergence sweep from 800 to 200 kHz during 1 ms, WURST sweep width of 1000 kHz (45 μs), 260 echoes, spikelet separation: 2967 Hz, number of VOCS offsets: 5, offset step: 100 kHz, 9600 scans per offset (~1 h 20 min), relaxation delay: 0.5 s, total experimental time: ~6 h 40 min. Partial excitation of the ST is observed at the ends of the spectrum. Vertical arrow: extra intensity when compared to the simulated spectrum, in red (pure quadrupolar lineshape with: C_Q = 31.5 MHz, η_Q = 0.80, δ_{iso} = 0.0 ppm) (see text and Figure S5). (b) Estimation of C_Q for Sr-malonate (fixed η_Q = 0.80).

The static ^{87}Sr NMR spectra of Sr-organic complexes, Sr-phenylboronate (Figure S7), and Sr phenylphosphonate (Figure S8) were then recorded at natural abundance using a DFS−WURST−QCPMG experiment. In both cases, the lineshape is characteristic of one unique crystallographic site, in agreement with XRD data (Figure S1). By simulating the spectra (neglecting CSA contributions), the NMR parameters obtained for the Sr-phenylboronate were C_Q = 20.2 ± 0.7 MHz, η_Q = 0.25 ± 0.10, δ_{iso} = 50 ± 60 ppm, and for the Sr-phenylphosphonate C_Q = 34.5 ± 0.7 MHz, η_Q = 0.65 ± 0.10, δ_{iso} = 0 ± 200 ppm. A distortion of the lineshape was observed for the Sr-phenylphosphonate near −4000 ppm. It may be due to satellite interference, as suggested previously for Sr-malonate. However, it has to be emphasized that the S/N ratio for this particular sample was rather limited and that the "true" intensities of the individual spikelets may be affected by residual noise.

Crystalline Sr silicates and phosphates were then studied, in view of the investigations on the Sr-doped bioactive glasses. The ^{87}Sr NMR spectrum of SrSiO$_3$ (Figure S9) involves two crystallographic sites (one of these is represented in Figure S1). A quadrupolar lineshape related to a moderate C_Q is clearly observed (C_Q = 18.5 ± 0.5 MHz, η_Q = 0.45 ± 0.10, δ_{iso} = 0 ± 70 ppm, see the insert in Figure S9), which was further assigned to site 2 based on GIPAW calculations (see below). A second much broader component (corresponding to site 1) can also be observed using a QCPMG spikelet interval of 8547 Hz in the NMR experiment and is characterized by C_Q = 46.0 ± 1.0 MHz, η_Q = 0.40 ± 0.15, δ_{iso} = 0 ± 100 ppm (see Table 1). It has to be emphasized that potential contributions of the ST of site 2 may be overlapping with the broad resonance. In the case

12617

dx.doi.org/10.1021/ja303505g | *J. Am. Chem. Soc.* 2012, 134, 12611−12628

of α-SrP$_2$O$_6$, the lineshape is even more complex to analyze, as four crystallographic sites are involved in the structure (Figure S10). To estimate the C_Q, various simulations (with fixed η_Q = 0.0) were performed, revealing that $C_Q \sim 38$ MHz is a good estimate. From other numerical simulations, it was found that the range of C_Q values for the different sites is actually 32 MHz $\leq C_Q \leq 42$ MHz. However, at this stage, it is far more difficult to determine a range of η_Q values. A detailed simulation of this lineshape based on GIPAW calculations will be described below. It should be noted that like for the Sr-malonate compound, partial excitation of the ST was observed for large VOCS offsets for α-SrP$_2$O$_6$ (see Figure S11).

Protonated Sr-phosphates and hydrogen phosphates were also studied, as they may be representative of some of the environments found for Sr after reaction of bioactive glasses with SBF. A mixture of ^{87}Sr-labeled belovite (*Sr$_{10}$(PO$_4$)$_6$(OH)$_2$) and *SrHPO$_4$ was first analyzed (see Materials and Methods). Despite very long experimental time (>10 h), no significant signal was obtained (apart from a very few spikelets with very limited signal-to-noise ratio). Upon heating, the mixture of *Sr$_{10}$(PO$_4$)$_6$(OH)$_2$ and *SrHPO$_4$ was converted into another Sr phosphate, *Sr$_3$(PO$_4$)$_2$, which was phase pure and crystalline. For this phase (which contains exactly the same amount of ^{87}Sr isotope as in the previous mixture), the ^{87}Sr NMR spectrum was easily obtained, exhibiting an excellent signal-to-noise ratio (Figure S12); the two crystallographic sites (Table 1) are characterized by: C_Q = 30.5 ± 0.5 MHz, η_Q = 0.1 ± 0.1, δ_{iso} = 0 ± 100 ppm and C_Q = 69.0 ± 1.0 MHz, η_Q = 0.1 ± 0.1, δ_{iso} = 0 ± 200 ppm. The huge difference in S/N between the {*Sr$_{10}$(PO$_4$)$_6$(OH)$_2$ and *SrHPO$_4$} and *Sr$_3$(PO$_4$)$_2$ samples could indicate the necessity of ^{1}H decoupling during the QCPMG acquisition for Sr-structures containing protons. Indeed, Rossini et al.[64] and O'Dell et al.[48] have demonstrated recently that CW ^{1}H decoupling could significantly lengthen the time for which echoes are acquired in the QCPMG experiment on quadrupolar nuclei, leading to clear improvement of the signal-to-noise ratio. Thus, we tested the efficiency of CW ^{1}H decoupling on the Sr-malonate and Sr-boronate samples (Figure S4c,d). In the case of Sr-malonate, the effect of proton decoupling is very limited, as it affects the signal intensity by less than 5%. In the case of Sr-boronate, no clear effect is observed on the intensity of the echoes in the time domain nor on the final spectra.[88] In other words, low power ^{1}H decoupling (here ~15 kHz) has almost no influence on the signal-to-noise ratio. It is possible that protons affect the relaxation of ^{87}Sr, leading to a much shorter T_2 and thereby greatly decreasing the intensity of the echoes. To confirm this assumption, a partly deuterated Sr-phenyl-boronate sample was synthesized (see Supporting Information). The comparison between the ^{87}Sr NMR spectra of H- and D- Sr-phenylboronates (recorded using the same mass of samples) is presented in Figure S4e, revealing a slightly increased S/N ratio upon deuteration (by a factor of ~1.4 on average). Therefore, it appears that the substitution of protons by deuterium has some beneficial effect on the detection of the ^{87}Sr NMR signal. As detailed later in the manuscript, this led us to investigate the structural changes of the B75-Sr10-bioactive glass upon immersion in SBF using SBF prepared with D$_2$O instead of H$_2$O. Finally, it should be noted that the role of protons in ^{87}Sr NMR spectroscopy was further examined by recording the ^{87}Sr NMR spectra of fluorinated analogues of some of the OH containing phases studied here or by carrying out ^{87}Sr NMR experiments at 100 K (data not shown). The

preliminary results demonstrated unambiguously that ^{87}Sr NMR spectra are more readily recorded when OH groups are substituted by fluorine anions. However, for belovite (containing only OH groups), no significant improvement in signal-to-noise was observed at very low temperature.

In conclusion of this in-depth study of ^{87}Sr NMR spectroscopy, the following points summarize how to approach ^{87}Sr NMR experiments: (i) the first offset can be set at 0 ppm, as isotropic chemical shift and CSA effects can be neglected as a first approximation (see GIPAW calculations below); (ii) for a given offset, when combining DFS, WURST irradiation, and QCPMG, the first spikelets of the spectrum are generally observed after a maximum ~1 h of acquisition at 19.8 T for crystalline materials; (iii) if $C_Q \leq 65$ MHz, five to seven offsets (with 100 kHz steps) are sufficient to cover the whole lineshape at ultra high magnetic field (here 19.8 T); (iv) for H-containing structures, {^{1}H} decoupling at 15 kHz is inefficient, but deuteration can be possibly helpful; (v) enriching samples in ^{87}Sr dramatically increases the signal-to-noise. For all crystalline samples described above, ^{87}Sr NMR parameters were determined by simulation of the static lineshapes. From the simulations, it clearly appears that the quadrupolar parameters (C_Q and η_Q) can be measured with much more precision than the isotropic chemical shifts because of the large quadrupolar interaction and a rather limited chemical shift range in comparison to the effect of C_Q. Furthermore, a wide range of C_Q values was observed (between 8 and 70 MHz), which suggests that these quadrupolar parameters may provide more information about the local environment of strontium than $\delta_{iso}(^{87}$Sr) (Table 1).

GIPAW Calculations of ^{87}Sr NMR Parameters. GIPAW calculations were performed using two calculation codes: PWSCF and CASTEP (Tables 1 and S2, respectively). The main goal of these calculations was to see whether calculations could closely reproduce experimental ^{87}Sr NMR parameters (δ_{iso}, C_Q, η_Q, Δ_{CSA}, and η_{CSA}), in view of then performing such calculations on structural models of bioactive glasses.

As shown above, as well as in some of the very first ^{87}Sr NMR investigations,[39] experimental quadrupolar parameters of crystalline samples can be measured accurately. However, this is not always the case for δ_{iso}, meaning that to be able to fully validate the NMR calculations, a larger number of accurate experimental isotropic chemical shift values is needed. According to previous studies,[37] for compounds in which Sr has a "cubic" local environment such as SrO, SrCl$_2$, and SrF$_2$, isotropic chemical shifts can be measured with high accuracy (±2 ppm) from the sharpness of the NMR lines. As a result, to increase the number of experimental values of $\delta_{iso}(^{87}$Sr) available to help validate the calculations, the experimental MAS NMR spectra of two more samples with a "cubic" Sr local environment were recorded: SrS and SrB$_6$ (Figure S13). SrS is characterized by a very sharp isotropic line at δ_{iso} = 319.2 ± 0.5 ppm and a very small quadrupolar interaction, $C_Q \sim 0.3$ MHz, as shown by the corresponding spinning sideband pattern. Concerning SrB$_6$, a more detailed analysis of the ^{87}Sr MAS NMR spectrum was carried out using QUADFIT,[66] as shown in Figures S14 (MAS, 19.8 T) and S15 (static, 14.0 T). Because of reduced signal-to-noise ratio in the MAS data, the following conclusions were mainly derived from the static spectrum (Figure S15). Two components can be extracted: (i) a sharp one, with C_Q = 0.7 ± 0.4 MHz, η_Q = 0.2 ± 0.2, and δ_{iso} = 94.0 ppm, and (ii) a much broader one, with C_Q = 5.1 ± 0.5 MHz, η_Q = 0.2 ± 0.2 and δ_{iso} = 103.0 ppm, and a Gaussian

12618

dx.doi.org/10.1021/ja303505g | *J. Am. Chem. Soc.* 2012, 134, 12611–12628

distribution of C_Q (fwhh =3.6 ± 0.5 MHz). At this stage, the assignment of the two components is unclear, but the ^{87}Sr isotropic chemical shift for SrB$_6$ can be safely estimated as 100 ± 6 ppm. As a result, by comparing experimental and calculated δ_{iso} values (Figure S3b), it appears that isotropic chemical shifts can be calculated accurately. As mentioned previously, concerning all the other Sr compounds, most ^{87}Sr NMR static patterns are very broad and dominated by quadrupolar effects. Hence, the large uncertainties associated with the chemical shift extracted from the ^{87}Sr NMR spectra place severe limitations on using $\delta_{iso}(^{87}$Sr) with any sort of quantitative accuracy. Nevertheless, when looking at all the ^{87}Sr chemical shift calculations, it appears that the following experimental trends are correctly predicted by GIPAW (whether the calculations are performed by CASTEP or PWSCF, as shown in Tables 1 and S2): (i) SrS, SrO, and SrB$_6$ correspond to the sites which are the most deshielded in this series of compounds; (ii) for all derivatives, calculated anisotropies Δ_{CSA} are very small (≤170 ppm, Table 1), in agreement with the experimental data (see above and Figure S5).

The correlation between calculated (PWSCF) and experimental C_Q values is given in Figure 2 for SrB$_6$, SrCO$_3$,
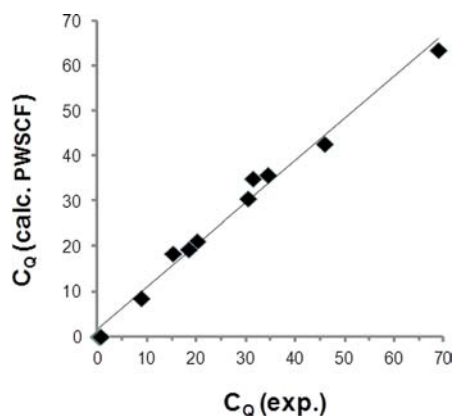
Figure 2. Experimental C_Q values (in MHz) vs GIPAW (PWSCF) data for SrB$_6$, SrCO$_3$, Sr(NO$_3$)$_2$, SrSiO$_3$, Sr$_3$(PO$_4$)$_2$, Sr-phenylboronate, Sr-malonate, and Sr-phenylphosphonate (see Table 1). The equation of the solid line is $y = 0.929x + 1.683$ ($R^2 = 0.987$).

Sr(NO$_3$)$_2$, SrSiO$_3$, Sr$_3$(PO$_4$)$_2$, Sr-malonate, Sr-phenylboronate, and Sr-phenylphosphonate. An excellent agreement is observed. The same trend is demonstrated using CASTEP but with slightly less accurate predictions and a more pronounced scattering of the data (see Figure S16). Most importantly, it appears that the GIPAW approach is suitable for the prediction of C_Q over the *whole range* observed so far, i.e., from ~0 to ~70 MHz. Possible relationships between C_Q and geometric features around Sr are discussed later. Concerning the quadrupolar asymmetry parameter, η_Q, it should be noted that predictions are reasonably accurate, except for SrCO$_3$ (PWSCF) and Sr-phenylboronate (η_{Qcalc} overestimated by both PWSCF and CASTEP).

To further demonstrate the strength of the GIPAW approach for the interpretation of complex ^{87}Sr NMR spectra, more comprehensive simulations of the spectrum of α-SrP$_2$O$_6$ (which has four crystallographic Sr sites) were performed (Figure S17). The GIPAW calculations (Table 1) show that $C_{Q(calc)}(^{87}$Sr) ranges between 32.9 and 40.8 MHz (nonrelaxed structures), in good agreement with estimates made previously (see above). Moreover, tensors are expected that tend toward more axial

values ($\eta_Q \leq 0.31$). As a matter of fact, when simulating the spectrum using four axial tensors (Figure S17b), the intensity in the central part of the spectrum (at $\delta \sim 0$ ppm) is underestimated. Therefore, it appears necessary to impose $\eta_Q \neq 0$ for at least one of the four sites. A reasonable simulation is given in Figure S17c, with the following set of $\{C_Q, \eta_Q\}$ parameters: {32.0 MHz, 0.80}, {38.0 MHz, 0.00}, {39.0 MHz, 0.00}, {40.7 MHz, 0.00}. This analysis shows that GIPAW predictions can thus clearly be used as a suitable starting point for the simulation of complex ^{87}Sr lineshapes corresponding to multisite structures.

As a summary of this subsection, it appears that predictions of ^{87}Sr quadrupolar parameters can be obtained through GIPAW calculations on a structural model of a material, for two different calculation codes, PWSCF and CASTEP. In particular, starting from GIPAW data, complex spectra involving multiple sites can be satisfactorily assigned. Moreover, GIPAW data are not only useful for a posteriori interpretation of experimental spectra but also help determine the set up of the ^{87}Sr experiments, following this empirical rule of thumb (for ultrahigh magnetic field, ~19.9 to 23.3 T): for $C_Q \leq 20$ MHz, one unique VOCS offset is necessary, whereas five to eight offsets are needed for $C_Q \geq 30$ MHz. This is of particular importance for structures characterized by very large C_Q constants such as Sr-malonate, Sr-phenylphosphonate, α-SrP$_2$O$_6$, SrSiO$_3$, and Sr$_3$(PO$_4$)$_2$.

Having implemented a new methodology to carry out ^{87}Sr NMR experiments and demonstrated the validity of GIPAW calculations, we then moved on to the characterization of B75-Sr10. The study of structural models of this bioactive glass are now possible.

Strontium Environments in Bioactive Glasses. *Experimental and Computational Study of Sr-Bioactive Glasses Using ^{87}Sr NMR.* The B75-Sr10 bioactive glass sample (76.9SiO$_2$−17.6CaO−5.5SrO, mol %) is challenging for natural abundance ^{87}Sr NMR spectroscopy. Indeed, the wt % of Sr is only ~9% (see Materials and Methods), leading to an intrinsically low ^{87}Sr signal-to-noise ratio. The natural abundance ^{87}Sr NMR static spectrum of the bioactive glass was recorded at 16.3 T and is presented in Figure 3 as an insert. Five different VOCS offsets were added to obtain this spectrum, for a total experimental time of ~57 h. Crude NMR parameters can be extracted by simulating the spectrum: $C_Q \sim 33$ MHz, $\eta_Q \sim 1$, $\delta_{iso}(^{87}$Sr) ~ 0 ppm (neglecting any potential distributions of the NMR parameters).

The broad lineshape observed in Figure 3 rules out the possibility of finding strontium in a highly symmetric SrO-type environment within the glass. However, the full interpretation of this spectrum presents a double challenge. (i) First, experimentally, the limited signal-to-noise ratio may have a strong influence on the intensities of the QCPMG spikelets, and this can be misleading when simulating the lineshape. Indeed, when looking at the ^{87}Sr NMR parameters calculated by GIPAW for crystalline Sr silicate phases (SrSiO$_3$, Sr$_3$SiO$_5$) and a Ca/Sr silicate phase (CaSrSiO$_4$), it appears that $C_Q(^{87}$Sr) values are highly distributed and can be very large, greatly exceeding 35 MHz (see Table 1). Assuming that Sr sites with such large C_Q values are also present in the bioactive glass, strongly broadened lineshapes would be expected in the spectrum with extremely weak spikelet intensities. Obviously, such lines could not be detected at natural abundance, and it would be unrealistic to try to detect them by increasing the experimental time, as 57 h were already needed for this
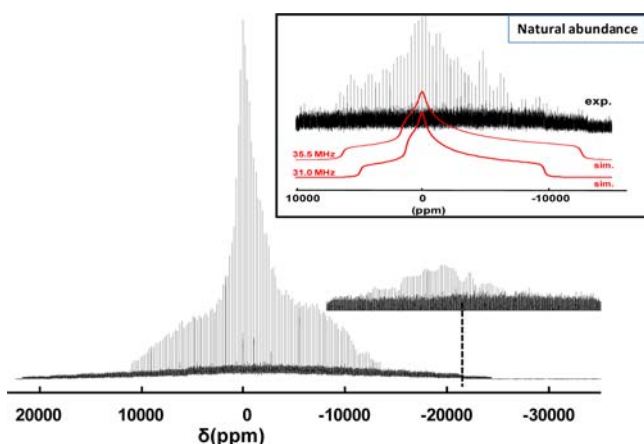
Figure 3. Inset: Static DFS−WURST−QCPMG ^{87}Sr NMR spectrum of the *nonlabeled* bioactive glass, B75-Sr10. Experimental parameters: 16.3 T, 5 mm Bruker static probe, DFS convergence sweep from 800 to 200 kHz during 1 ms, WURST sweep width of 500 kHz (45 μs), 260 echoes, spikelet separation: 8547 Hz, number of VOCS offsets: 5, offset step: 100 kHz, 122 000 scans per offset (∼11 h 20 min.), relaxation delay: 0.3 s, total experimental time: ∼57 h. Simulated spectra, in red: one unique quadrupolar site with C_Q = 31.0 and 35.5 MHz (fixed η_Q = 1.00, fixed δ_{iso} = 0.0 ppm). Spectrum: static DFS−WURST−QCPMG ^{87}Sr NMR spectrum of the *labeled* bioactive glass, B75-*Sr10. Experimental parameters: 19.8 T, 7 mm Bruker probe, DFS convergence sweep from 800 to 400 kHz during 1 ms, WURST sweep width of 1000 kHz (45 μs), 400 echoes, spikelet separation: 7874 Hz, number of VOCS offsets: 10, offset step: 100 kHz, 10 000 scans per offset (∼1 h), relaxation delay: 0.3 s, total experimental time: ∼10 h. The vertical dashed line corresponds to the largest offset: −800 kHz (or ∼−22 000 ppm).

spectrum. (ii) Second, to help interpret the ^{87}Sr NMR spectrum using GIPAW computations, structural models for the Sr-containing glasses are needed. Several models are necessary for a given glass composition to provide good statistics for the local environment of the Sr atoms. For each Sr site, GIPAW calculations can then be performed to extract ^{87}Sr C_Q, η_Q, and δ_{iso} values and then compare the computed and experimental data.

Point (i) was addressed by labeling the Sr-bioactive glass in ^{87}Sr (see Materials and Methods, B75-*Sr10). The corresponding ^{87}Sr DFS−WURST−QCPMG NMR spectrum is presented in Figure 3 (total experimental time: ∼10 h; 10 offsets were necessary here). It is clear that labeling in ^{87}Sr has a very significant effect on the signal-to-noise ratio. Most importantly, it allows the detection of the very broad components of the spectrum, which could not be detected at all in natural abundance (see the insert in Figure 3). The spectrum is characterized by a rather "sharp" component (from ∼−3500 ppm to ∼1500 ppm) superimposed on a much broader one

(from ∼−25 000 ppm to ∼12 000 ppm). At δ ∼−25 000 ppm (offset: −800 kHz), spikelets are still visible on the spectrum. Using DMFit[65] and standard simulations of a pure quadrupolar lineshape, the maximum experimental broadening observed here corresponds to C_Q > 70 MHz, which is higher than the largest C_Q values observed and/or calculated for crystalline $SrSiO_3$, Sr_3SiO_5, and $CaSrSiO_4$ phases (C_Q ≤ 53 MHz, see Table 1). In other words, a non-negligible fraction of the sites present which produce the broad line cannot be explained by a simple comparison with reference strontium silicates (which may come from both CT and ST contributions).

To assist in the interpretation of the ^{87}Sr NMR spectrum of the bioactive glass (point (ii) mentioned above), modeling of the Sr-doped glasses followed by GIPAW calculations were performed. Charpentier et al. were the first to propose such an approach for the study of vitreous silica,[89] sodium silicate glasses,[90] $CaSiO_3$[58] (starting here from experimental data published by Zhang et al.)[59] and fluoride-containing bioactive glasses:[91] for these glass compositions, distributions of Q^n, mean $\delta_{iso}(^{29}Si)$, and standard deviations were extracted theoretically and compared successfully to experimental ^{29}Si NMR data, providing direct insight into the structure of these complex phases at the atomic level. Here, we chose models of Sr-glasses with various compositions in the SiO_2−CaO−SrO (such as B75-Sr10), SiO_2−SrO and also SiO_2−Na_2O−CaO−SrO−P_2O_5 phase diagrams, as further explained below. These models were obtained from MD simulations and optimization by first principles DFT (see Materials and Methods and Table S1). Information on their structure (Q^n distributions for the Si units and coordination environment of Sr) is given in Tables 2, 3, and S3 and discussed in the following paragraphs. The ^{87}Sr and ^{29}Si NMR data were then calculated by GIPAW for these models (see Figure 4 and Tables 2, S3, and S4) and compared to experimental data on B75-Sr10 and other Sr-bioactive glasses.[92]

As a starting point of the computational study, we looked into the effects of Sr substitution on the structure of the 45S5 Bioglass to validate our computational approach. Although these phases have a chemical composition which does not correspond exactly to that of B75-Sr10 (as they are based on sodium calcium phosphosilicate glasses), they are directly related to the 45S5 bioglasses first introduced by Hench and co-workers,[67] which have already been investigated by MD[23] and which are considered as the golden standard in the field. For one model of Sr−substituted Hench glass of composition 46.1SiO_2−24.4 Na_2O−16.9CaO−10SrO−2.6 P_2O_5 (mol %), ^{29}Si NMR data were calculated by GIPAW (Table S3).[93] For Q^1, Q^2, and Q^3 units, the mean values of calculated ^{29}Si NMR chemical shifts were −68.1, −78.6, and −86.3 ppm, respectively, and a majority of Q^2 species was observed. These observations are in agreement with previously reported

Table 2. Q^n Distributions and GIPAW Calculated ^{29}Si NMR Data for the 76.9SiO_2−17.6CaO−5.5SrO and 93.4SiO_2−6.6SrO Glass Models[a]

glass model	Si	Q^0	Q^1	Q^2	Q^3	Q^4
93.4SiO_2-6.6SrO	Q^n distribution (%)	0.0	0.0	0.0	15.6 (0.0)	84.4 (0.0)
	mean $\delta_{iso}(^{29}Si)$ (ppm)	–	–	–	−101.1 (9.5)	−111.2 (6.4)
76.9SiO_2-17.6CaO-5.5SrO	Q^n distribution (%)	0.0	1.4 (2.3)	6.4 (3.9)	40.0 (9.3)	52.1 (5.4)
	mean $\delta_{iso}(^{29}Si)$ (ppm)	–	−79.8 (6.6)	−86.9 (5.5)	−97.0 (6.6)	−110.8 (6.6)

[a]The information was averaged over all the different Si sites in the five different computational models of each glass. Standard deviations are given in parentheses. Each simulated model contained ∼200 atoms per simulation cell.

12620

dx.doi.org/10.1021/ja303505g | *J. Am. Chem. Soc.* 2012, 134, 12611−12628

Table 3. Sr (and Ca) Environments in the 76.9SiO$_2$–17.6CaO–5.5SrO and 93.4SiO$_2$–6.6SrO Glass Models^a

glass model	93.4SiO$_2$–6.6SrO	76.9SiO$_2$–17.6CaO–5.5SrO
	Sr Environment	
average Sr CN	7.2 (0.6)^b (cutoff = 3.67 Å)	6.4 (0.5)^c (cutoff = 3.55 Å)
average contribution to CN		
from BO	56.7%	33.6%
from NBO	43.3%	66.4%
average angles		
O–Sr–O (°)	99.0 (39.6)	100.1 (34.0)
BO–Sr–BO (°)	86.9 (5.0)	89.9 (8.0)
BO–Sr–NBO (°)	103.1 (37.1)	101.5 (37.5)
NBO–Sr–NBO (°)	102.0 (20.8)	100.8 (10.2)
	Ca Environment	
average Ca CN	–	5.5 (0.1) (cutoff = 3.17 Å)
average contribution to CN		
from BO		31.5%
from NBO		68.5%
average angles		
O–Ca–O (°)		101.9 (25.4)
BO–Ca–BO (°)		90.3 (5.2)
BO–Ca–NBO (°)		102.1 (32.4)
NBO–Ca–NBO (°)		104.2 (18.4)

^{a}The information was averaged over all the different Sr sites in the five different computational models of each glass. Standard deviations are given in parentheses. Each simulated model contained ~200 atoms per simulation cell. ^{b}Average over a total of 25 Sr sites (five sites per model, five models). ^{c}Average over a total of 20 Sr sites (four sites per model, five models).

^{29}Si NMR characterizations of Sr-substituted Hench-like bioactive glasses prepared by the melt-and-quench procedure,[16,17] and are also in very good agreement with the GIPAW computed data obtained recently by Charpentier et al. on models of nonsubstituted 45S5 bioglasses (−70.7, −79.5, and −87.0 ppm, respectively).[94] Thus, this suggests that our overall approach for modeling and studying Sr-substituted glasses is valid from the NMR point of view, and that it can be applied to Sr-bioactive glasses such as B75-Sr10.

The Sr-bioactive glass B75-Sr10 studied here has the composition 76.9SiO$_2$–17.6CaO–5.5SrO, mol %. Five models of the glass corresponding to this composition were thus generated computationally by the melt-and-quench glass formation process (Tables 2 and 3). As B75-Sr10 was obtained by the *sol–gel process* (and not by a melt-and-quench synthetic procedure), possible variations of composition corresponding to partial phase separation of *nano*domains were anticipated. Five models of composition 93.4SiO$_2$–6.6SrO were therefore also computed (by setting Sr/Si = 0.07, which is the same value as in B75-Sr10). In this case, it is assumed that all Sr atoms are inserted in a silica-rich phase. The fully relaxed ^{29}Si MAS NMR spectrum of B75-Sr10 is presented in Figure 4a, together with the calculated ^{29}Si NMR data corresponding to the five models of 76.9SiO$_2$–17.6CaO–5.5SrO (280 Si units in total) and 93.4SiO$_2$–6.6SrO (320 Si units in total) (see Table 2 for mean values of the calculated ^{29}Si NMR chemical shifts and their

associated standard deviations).[95] Interestingly, Figure 4a suggests that the sol–gel bioactive glass B75-Sr10 is closer to the 93.4SiO$_2$–6.6SrO model from the ^{29}Si NMR point of view. Indeed, only one major peak centered at δ ~−110 ppm is observed (corresponding mainly to Q^4 and Q^3 units), whereas Q^1 and Q^2 units are present in much smaller proportions. This unexpected observation could mean that a phase segregation has occurred during the sol–gel synthesis of B75-Sr10, leading to the formation of Sr-silicate-like nanodomains.

Strontium local environments in the different models were then analyzed. A total of 20, 25, and 35 Sr sites are present in the 76.9SiO$_2$–17.6CaO–5.5SrO, 93.4SiO$_2$–6.6SrO, and 46.1SiO$_2$–24.4Na$_2$O–16.9CaO–10.0SrO–2.6P$_2$O$_5$ models, respectively. The coordination of Sr ranges from 5 to 10, in agreement with standard coordination numbers observed in crystalline Sr compounds (see above and Figure S1). The average coordination number (CN) differs from one model to the other (Tables 3 and S3), as well as the distribution between the different coordination numbers. For example, the 6-fold coordination is observed for ~50% of the Sr sites in the 76.9SiO$_2$–17.6CaO–5.5SrO composition, and for ~32% of the Sr sites in 93.4 SiO$_2$–6.6 SrO. The comparison of the strontium environments in the 76.9SiO$_2$–17.6CaO–5.5SrO and 93.4SiO$_2$–6.6SrO compositions also shows clear differences in the local structure around Sr (Table 3 and Figure S18), with more bridging oxygens (BO) and less nonbridging oxygens (NBO) bound to the cation in 93.4SiO$_2$–6.6SrO, meaning that the structural role of Sr in both glasses is clearly different. In addition, the comparison of the Ca and Sr local environments in 76.9SiO$_2$–17.6CaO–5.5SrO reveals marked differences in average coordination numbers around the metal (5.5 vs 6.4). Thus, from all these different models, it seems clear that (i) a wide variety of Sr local environments can a priori be expected in bioactive glasses, depending on the glass composition, and that (ii) Sr does not necessarily play the same structural role as Ca in glass networks, as previously observed in the glass models of the Sr-substituted 45S5 developed by Du et al.[23]

To determine which of the 76.9SiO$_2$–17.6CaO–5.5SrO or 93.4SiO$_2$–6.6SrO glass models provides a better description of Sr local environments in B75-Sr10, the ^{87}Sr NMR parameters of each of the Sr sites of five models (all calculated using GIPAW) were analyzed (see Table S4 for C_Q and η_Q values). Sr nuclei in these glass models are characterized by a very large distribution of quadrupolar constants, C_Q, ranging from ~25 to ~75 MHz. The C_Q ranges are comparable for the various glass compositions, as well as the mean C_Q values and associated standard deviations (in parentheses), which are 51.6 (11.8) and 46.7 (15.6) for 76.9SiO$_2$–17.6CaO–5.5SrO and 93.4SiO$_2$–6.6SrO compositions, respectively. However, the simulations of the *overall* quadrupolar lineshapes for the models of 76.9SiO$_2$–17.6CaO–5.5SrO or 93.4 SiO$_2$–6.6 SrO glasses reveal differences, as shown in Figures 4b and 5. From these observations, several comments can be made. (i) There is a clear qualitative agreement between the GIPAW computed C_Q data and the overall width of the experimental lineshape. In particular, the largest predicted C_Q values (~75 MHz) can explain nicely the broad components of the spectrum with the lowest intensity. Moreover, the "sharp" component centered at δ ~ 0 ppm can be safely assigned to moderate quadrupolar constants (~25 MHz $\leq$ C_Q $\leq$ ~35 MHz), which are systematically present in the glass models. (ii) The largest C_Q constants exceed by far those observed for crystalline Sr and
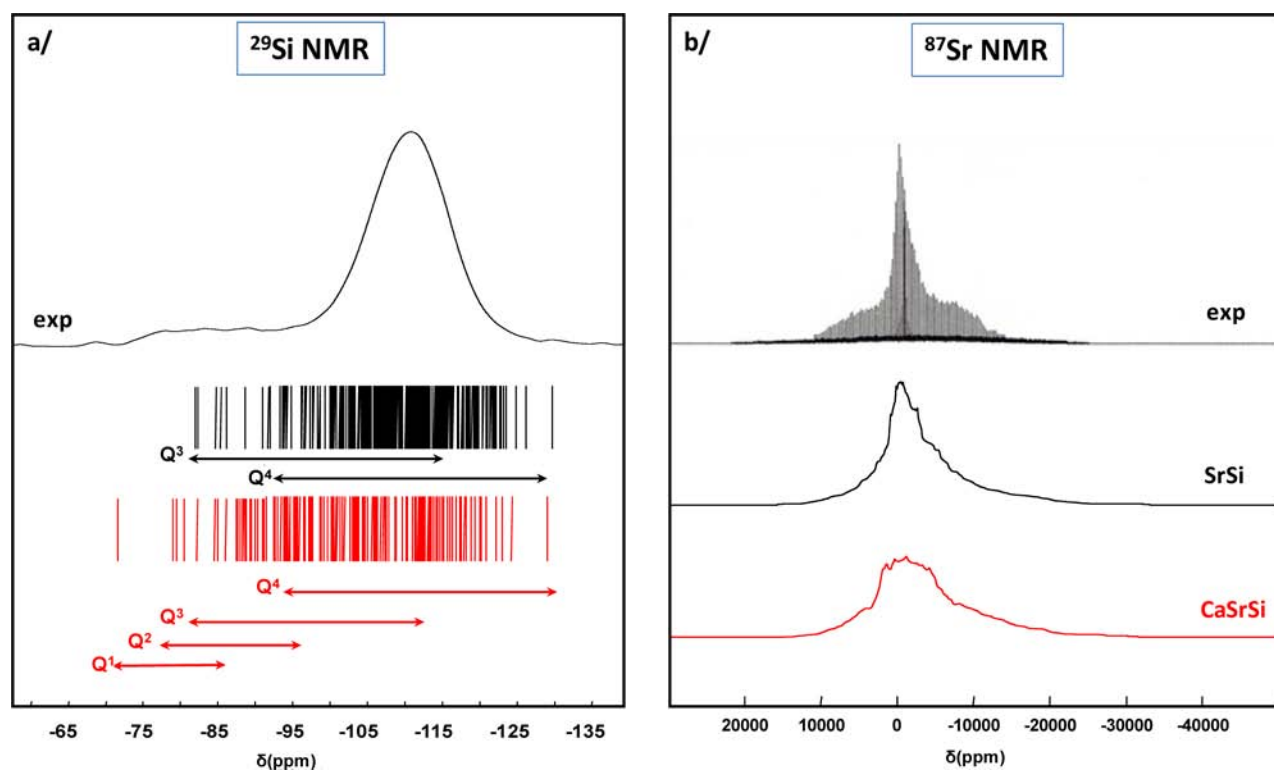
Figure 4. (a) ^{29}Si MAS NMR spectrum of B75-Sr10 (Experimental parameters: 7 T, 7 mm Bruker MAS probe, rotation frequency: 5 kHz, $t_{90°}(^{29}$Si) = 4.6 μs, pulse angle: 45°, relaxation delay: 300 s, 458 scans (~38 h); reference: TMS at 0 ppm), and GIPAW predictions of ^{29}Si NMR chemical shifts from the glass models (vertical bars at the bottom: black vertical bars for GIPAW predictions for the five models of composition 93.4 SiO$_2$–6.6 SrO, and red vertical bars for GIPAW predictions for the five models of composition 76.9SiO$_2$–17.6CaO–5.5SrO). The ranges for Q^n units are shown (see Table 2 for mean values and standard deviations). (b) Simulations (pure quadrupolar lineshapes) corresponding to *all* the ^{87}Sr sites in the glass models of composition 76.9SiO$_2$–17.6CaO–5.5SrO (CaSrSi) and 93.4 SiO$_2$–6.6 SrO (SrSi), respectively. The ^{87}Sr quadrupolar constants are given in Table S4. The experimental spectrum corresponds to the labeled B75-*Sr10 glass sample (see Figure 3).

Ca/Sr silicates such as Sr$_3$SiO$_5$ and CaSrSiO$_4$ (Table 1). In other words, the interpretation of the spectrum of B75-*Sr10 cannot be deduced simply by starting from the ^{87}Sr NMR parameters of related crystalline phases. (iii) It is clear from the simulations in Figure 5 that each glass model, taken individually, cannot account for the experimental ^{87}Sr NMR lineshape, and that many more Sr sites need to be taken into account for each composition. The number of Sr sites in the proposed models (20 to 25 in total) is probably still not sufficient to fully describe the Sr environments in the glass models.[96] Quantitative distributions for C_Q and η_Q were not extracted from the spectrum of B75-*Sr10. Nevertheless, from the calculated data currently available, it seems clear that when summing for each glass composition *all* the ^{87}Sr contributions of each site (i.e., 20 and 25 in total for 93.4 SiO$_2$–6.6 SrO and 76.9SiO$_2$–17.6CaO–5.5SrO, respectively), the ^{87}Sr NMR lineshape of B75-Sr10 appears to be more similar to the one observed in the 93.4 SiO$_2$–6.6 SrO models than in 76.9SiO$_2$–17.6CaO–5.5SrO, as it reproduces better the central sharper feature of the spectrum (Figure 4b). This would be in line with the previous conclusions drawn here from ^{29}Si NMR, which suggest that Sr is in a Sr-silicate-rich phase in B75-Sr10, following a phase segregation into nanodomains. All in all, this demonstrates that the combination of ^{87}Sr NMR and computational modeling (followed by GIPAW calculations) can provide direct insight into the local structure around Sr in bioactive glasses.

The very large C_Q range observed experimentally and satisfactorily predicted by GIPAW calculations raises the following question: is it actually possible to correlate the C_Q variations with local geometrical distortions around the Sr nuclei? This would allow structural information to be simply derived from the experimental ^{87}Sr NMR spectrum, without having to proceed to extensive and computationally demanding simulations. However, in contrast with quadrupolar nuclei such as ^{27}Al,[40,97] no clear trend relating $C_Q(^{87}$Sr) and shear or longitudinal strain parameters could be found, whether considering the Sr sites in the glass models or in the crystalline phases described above. No relationship between C_Q and coordination number of Sr in the glasses could be established either (see Figures 6 and S19). A more general concept previously proposed for the study of cationic environments in glasses was also investigated in view of trying to establish correlations, which consists of describing locally the symmetry of the Sr–O polyhedron (regardless of the coordination number) through the calculation of electric dipole[98] and quadrupole (λ_i, i = 1, 2, 3) moments[99] (the mathematical expressions for these dipole and quadrupole moments being given in ref 100). In Figure S20, the quadrupole moments λ_i are plotted vs C_Q for all Sr sites in a 6-coordinate environment in the 76.9SiO$_2$–17.6CaO–5.5SrO and 93.4SiO$_2$–6.6 SrO compositions. Clearly, there is no one to one correspondence between λ_i and the magnitude of C_Q, meaning that simple geometrical rules cannot be used to account for the evolution of C_Q from one site to the other. We believe that this is due to the nature of Sr–O bonds, which are predominantly ionic and poorly directional.[101] This proves that in the case of ^{87}Sr NMR, the interpretation of complex spectra strongly relies on
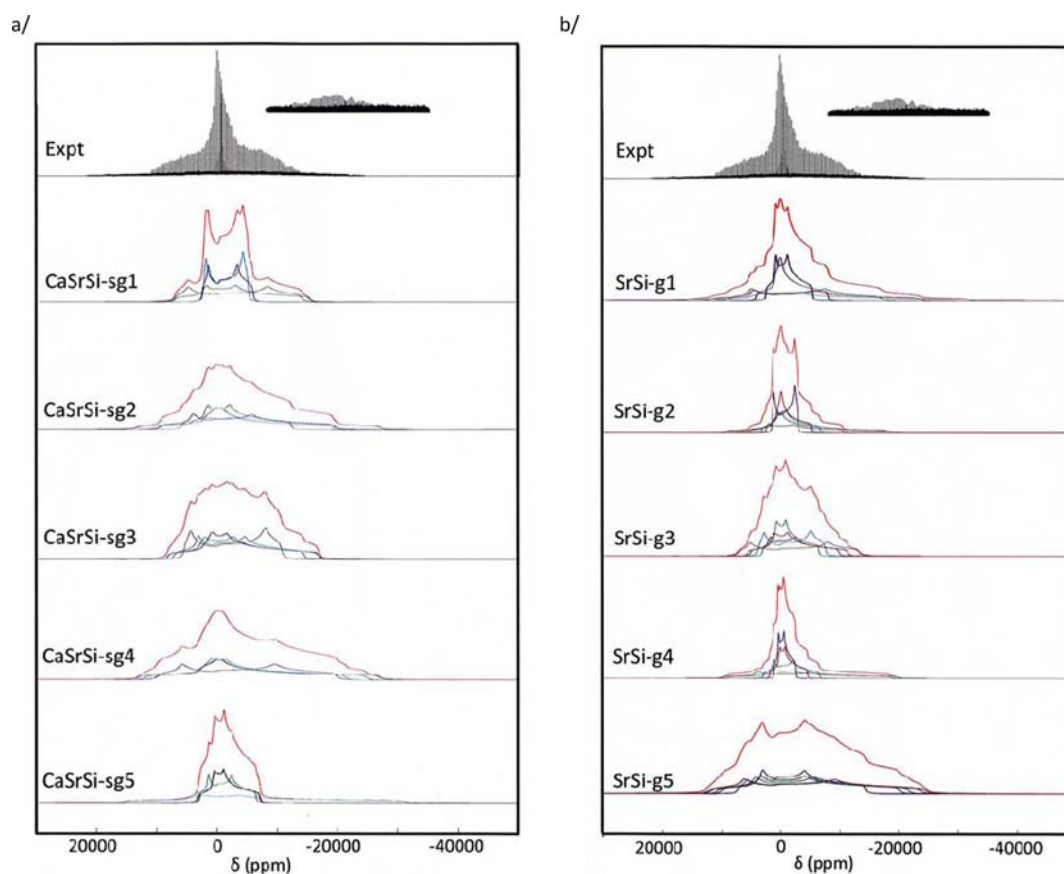
Figure 5. Simulations (pure quadrupolar lineshapes) corresponding to the ^{87}Sr sites in the individual glass models of composition (a) $76.9SiO_2-17.6CaO-5.5SrO$ (five models named CaSrSi-sgi) and (b) $93.4 SiO_2-6.6 SrO$ (five models named SrSi-gi). The ^{87}Sr quadrupolar constants are given in Table S4. The experimental spectrum corresponds to the labeled B75-*Sr10 glass sample (see Figure 3).
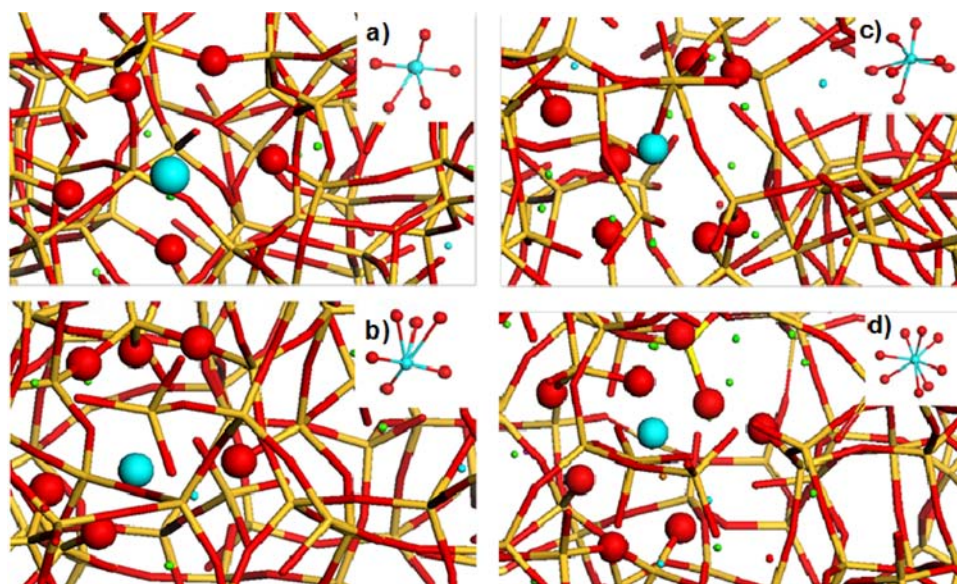

Figure 6. Strontium environments in $76.9SiO_2-17.6CaO-5.5SrO$ glass models a–d (representative five to eight coordination environments). Large light blue balls: Sr; large red balls: coordinated O around Sr; small green balls: Ca; small light blue balls: Sr. The yellow and red sticks show tetrahedral environments of the silicon oxygen network structure. Inserts: Sr and coordinated O only. (a) 5-fold coordination, C_Q = 51.4 MHz. (b) 6-fold coordination, C_Q = 60.4 MHz. (c) 7-fold coordination, C_Q = 64.9 MHz. (d) 8-fold coordination, C_Q = 35.6 MHz.

computational simulations, such as the ones we have described here.

In conclusion of this investigation of Sr local environments in bioactive glasses, it has been demonstrated that MD/DFT

modeling is a unique approach for visualizing the Sr–O polyhedra in a bioactive glass (Figure 6) and also for assisting in the interpretation of the corresponding ^{87}Sr NMR spectrum through the GIPAW approach. The C_Q range was found to be

B75-*Sr10 *after* immersion in SBF exp. time: ~ 16 h
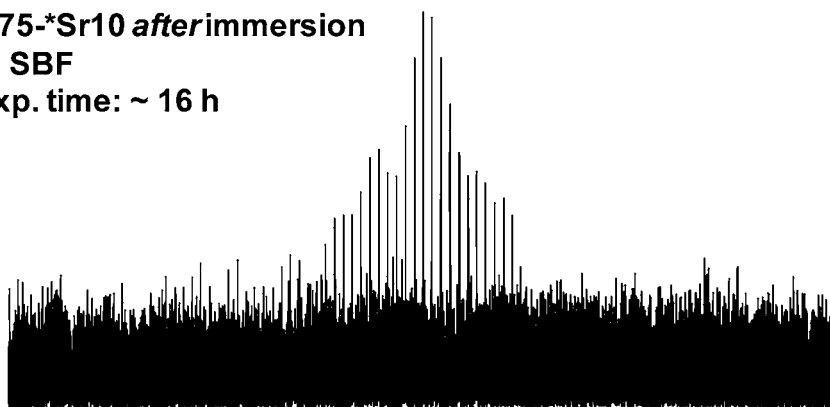
B75-*Sr10 *before* immersion in SBF exp. time: ~ 1 h
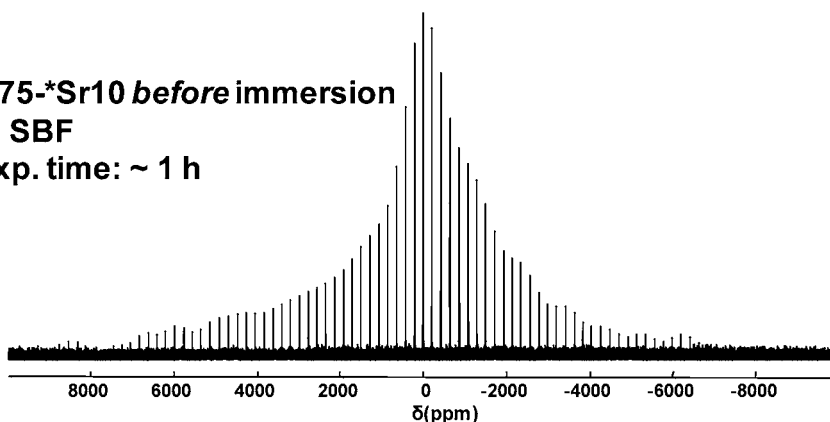
Figure 7. DFS−WURST−QCPMG [87]Sr NMR spectrum of labeled B75-*Sr10 *after* immersion (7 days) in SBF−D_2O. Experimental parameters: 19.8 T, 7 mm Bruker probe, DFS convergence sweep from 800 to 400 kHz during 1 ms, WURST sweep width of 1000 kHz (45 μs), 400 echoes, spikelet separation: 7874 Hz, number of VOCS offsets: 1, 160 000 scans (~16 h), relaxation delay: 0.3 s. Part of the spectrum of B75-*Sr10 *before* immersion in SBF−D_2O is presented for comparison (one offset, total experimental time: ~1 h).

very large and was accounted for using the glass models. Most importantly, in the case of B75-Sr10, comparisons of calculated and experimental [87]Sr and ^{29}Si NMR data suggest that phase segregation has occurred on the nanoscale during the synthesis. This new information about potential nanostructures in Sr-bioactive glasses is of interest when considering other Sr-bioactive glass phases prepared by sol−gel, because it could be one of the reasons for the differences in reactivity observed so far in the literature. Similar studies on other glass structures of different composition would thus be worth carrying out.

[87]Sr NMR Analysis of the Structural Changes in Bioactive Glasses upon Immersion in SBF. After implantation in the body, the distribution and local environments of Sr in the glass will change, allowing Sr to be released in body fluids. Here, the interaction of labeled B75-*Sr10 with SBF was thus monitored by [87]Sr NMR to see if structural changes could be observed. To minimize the potential effects of protons on T_2([87]Sr) relaxation (see above), d-SBF (i.e., SBF prepared in D_2O) was used as an immersion medium. Indeed, the Ca phosphate phases which will form upon immersion and the hydrated glass are expected to contain protons. After 7 days of immersion, the chemical composition of the reacted glasses and residual SBF solutions were analyzed, showing that ~80% of the Sr content had been released into solution. The DFS−WURST−QCPMG [87]Sr NMR spectrum of the B75-*Sr10 bioactive glass recovered after immersion is presented in Figure 7 for one WURST offset (total experimental time: ~16 h). When comparing it to the

spectrum of B75-*Sr10 *before* immersion in SBF, we see a dramatic decrease of the signal-to-noise ratio. This decrease exceeds by far the expected signal-to-noise ratio considering that 20% of Sr ions remain in the glass grains *after* immersion in SBF.[102] In other words, the [87]Sr NMR experiment is not able to detect all Sr nuclei in the sample.

A likely explanation for this observation is the following. Upon immersion in SBF, a phosphocalcic layer forms at the B75-*Sr10/SBF interface, which was easily identified as hydroxyapatite (HAp) by standard ^{31}P MAS and [1]H−^{31}P 2D CP MAS NMR experiments (Figure S21).[103,104] This HAp surface layer is likely to contain Sr^{2+} as a substitution for Ca^{2+} in the HAp phase. Indeed, μ-PIXE (particle-induced X-ray emission) quantitative chemical imaging reveals that after 7 days of interaction with SBF, Sr diffuses from the original glassy matrix to the mineralized surface layer which is only a few micrometers thick (see Figure S22). The chemical composition of this surface layer is found to be close to apatite, with an atomic Ca/P ratio of 1.68 (vs 1.67 for stoichiometric nonsubstituted HAp). The Sr concentrations in the mineralized surface layer were measured by μ-PIXE as 5.2 wt %, compared to 1.9 wt % in the core of the glass grains (a value which is in reasonable agreement with the ~1.5 wt % determined by ICP-AES). This implies that most of the Sr is probably present in the newly formed HAp phase.[105] Thus, despite the use of deuterated SBF, which might have helped slightly improve the signal-to-noise ratio (as demonstrated above for Sr-phenyl-

boronate), it is likely that the ^{87}Sr NMR signals coming from Sr atoms in the HAp surface layer are not detected, because when Sr is surrounded by protons or deuterium (especially coming from OH/OD groups or H_2O/D_2O molecules), ^{87}Sr signals can be more challenging to observe because of T_2 effects (see above the study of $SrHPO_4$ and belovite). This is also true for Sr sites which would be in the core of the eroding glass in hydrated environments, as water molecules are expected to migrate within the glass because of this erosion. Thus, we believe that the ^{87}Sr NMR spectrum recorded after immersion in d-SBF (Figure 7) is representative of only the Sr nuclei located in the *core* of the glass grains in *nonhydrated* and *nonhydroxylated* environments. To observe the hydrated/hydroxylated Sr-environments, other sequences such as ^{1}H–^{87}Sr CP QCPMG may be more appropriate. Indeed, in the case of ^{25}Mg NMR (^{25}Mg also being a low-gamma quadrupolar nucleus of low natural abundance), Davis et al. have shown that the Mg environments which appear upon dissolution of Mg-silicates can be detected using ^{1}H–^{25}Mg CP QCPMG.[106] However, such experiments were not attempted here and will be investigated in future studies.

As a conclusion of this section, it has been demonstrated that ^{87}Sr NMR spectroscopy in combination with chemical analyses, as well as ^{31}P and ^{1}H solid-state NMR, is a valuable tool of investigation for the detailed study of Sr bioavailability in glasses. After immersion in SBF, ^{87}Sr NMR is mostly sensitive to Sr nuclei located in the core of the glass grains in nonhydrated/hydroxylated environments. The fact that such environments are still detected after 7 days of immersion means that some portions of the initial glass have remained intact, containing residual Sr which can still be released. This is actually an important observation in itself, as it suggests that the stimulation of osteoblasts can occur over a fairly long period of time, which may ensure the proper osteointegration of the bioactive glass at the implantation site in the body, by formation of new bone tissue.

■ CONCLUSION

In this paper, a major step forward in the development of ^{87}Sr solid-state NMR spectroscopy has been made, from both experimental and computational points of view, to demonstrate that this technique can now be used to shed light on the local environment of strontium in complex materials of biomedical interest: Sr-containing bioactive glasses. Experimentally, it has been shown that the inherent drawbacks of ^{87}Sr (low γ and low natural abundance) can be circumvented by the combination of ultrahigh field magnets and specific pulse sequences (DFS, QCPMG, and WURST excitation). Indeed, natural abundance ^{87}Sr solid-state NMR spectra can now be recorded in reasonable time from many samples. ^{87}Sr GIPAW calculations (obtained using PWSCF or CASTEP codes) were found to show excellent agreement with trends observed experimentally for quadrupolar parameters. It was shown that quadrupolar coupling constants C_Q as large as 75 MHz can be expected, this interaction then being the dominant experimental broadening for such spectra. No clear trends relating quadrupolar parameters to local Sr environments could be established, meaning that to interpret complex ^{87}Sr NMR spectra, it is necessary to be able to model Sr-containing materials to then calculate the ^{87}Sr NMR parameters for these models using GIPAW.

Based on these new developments of ^{87}Sr NMR spectroscopy, the study of the structure of a bioactive Ca,Sr-silicate glass (B75-Sr10) was carried out. It was demonstrated that labeling in ^{87}Sr is a prerequisite to obtain reliable experimental spectra for such materials, as some spectral components are highly broadened by very large second-order quadrupolar effects. The ^{87}Sr NMR spectrum of B75-Sr10 was then analyzed and discussed using a combined experimental/modeling approach, as the experimental lineshape could not be interpreted on its own. Several computational models of the glass were proposed, corresponding to either Ca,Sr-silicate or Sr-silicate compositions. After optimization of the structure of each of these models at both MD and DFT levels, GIPAW calculations of C_Q were carried out, and the calculated values were compared to experimental data. Most interestingly, it was found that the Sr-silicate models are more similar to B75-Sr10 (from the ^{29}Si and ^{87}Sr NMR perspectives), which suggests that some phase segregation at the nanoscale may occur in the material. Such structural features, which had never been established previously, could be of importance, as they would provide new insight into the differences in reactivity of these materials. Finally, the bioavailability of Sr in the bioactive glasses was also studied by ^{87}Sr solid-state NMR, by analyzing the solid recovered after immersion of B75-Sr10 in a model physiological fluid. In that particular case, it was found that ^{87}Sr NMR is sensitive only to the Sr nuclei remaining in the core of the glass grains in nonhydrated/hydroxylated environments, and that such environments are still present (though in small quantities) after 1 week of immersion. A systematic comparison of changes in Sr environments in Sr-bioactive glasses of different compositions would be worth carrying out in the future at different stages of the release, as this should provide additional unprecedented insight into the bioavailability of the cation and release mechanism.

Beyond the application to pharmaceutical and biomedical materials, we believe that the developments made in this manuscript in ^{87}Sr solid-state NMR will also find a wide range of applications in other fields of materials science. Indeed, several other strontium materials have important applications in microelectronics, thermoelectric, nuclear waste storage, or superconducting devices,[107] and there are still unanswered questions about Sr environments in these phases.

■ ASSOCIATED CONTENT

ⓢ Supporting Information

Synthetic procedures for the preparation of Sr-phenylphosphonate and $Sr(C_6H_5B(OD)_3)_2 \cdot D_2O$. Figure S1: Representation of the chemical environment around Sr in $SrCO_3$, $Sr(NO_3)_2$, Sr-malonate, Sr-phenylboronate, Sr-phenylphosphonate, α-SrP_2O_6, $Sr_3(PO_4)_2$, and $SrSiO_3$. Figure S2: Powder XRD and IR data for SrB_6, α-SrP_2O_6, Sr−phenylphosphonate, Sr−malonate, $SrSiO_3$, $Sr(C_6H_5B(OH)_3)_2 \cdot H_2O$, $Sr(C_6H_5B-(OD)_3)_2 \cdot D_2O$, and $Sr_3(PO_4)_2$. Figure S3: (a) $\delta_{iso}(^{87}Sr)$ correlation between PWSCF and the experimental data for SrO and SrB_6. (b) $\delta_{iso}(^{87}Sr)$ correlation between CASTEP and the experimental data for SrO, SrS, SrB_6, SrF_2, and $SrCl_2$. Figure S4a: Static DFS−WURST−QCPMG ^{87}Sr NMR spectrum of Sr−malonate at 14.0 T and a unique offset vs the corresponding static DFS−QCPMG spectrum without WURST excitation. Figure S4b: Effect of DFS on Sr−malonate. Effect of ^{1}H decoupling (CW mode) on Sr−malonate (Figure S4c) and Sr−boronate (Figure S4d). Figure S4e: Effect of

deuteration on Sr−boronate. Figure S5: Potential effect of ^{87}Sr CSA on the static lineshape, for fixed C_Q, η_Q, δ_{iso}, η_{CSA}. Figure S6: Simulation of a pure ^{87}Sr quadrupolar lineshape for C_Q = 31.5 MHz, η_Q = 0.80, δ_{iso} = 0.0 ppm: CT simulation and full simulation (including CT and all ST). Figure S7: Static DFS−WURST−QCPMG ^{87}Sr NMR spectrum of Sr(C_6H_5B-$(OH)_3)_2 \cdot H_2O$ (19.8 T). Figure S8: Static DFS−WURST−QCPMG ^{87}Sr NMR spectrum of Sr($C_6H_5PO_2(OH))_2$ (19.8 T). Figure S9: ^{87}Sr and ^{29}Si NMR data for SrSiO$_3$. Figure S10: Static DFS−WURST−QCPMG ^{87}Sr NMR spectrum of α-SrP$_2$O$_6$ (19.8 T). Figure S11: Static DFS−QCPMG ^{87}Sr NMR spectrum of α-SrP$_2$O$_6$. Figure S12: DFS−WURST−QCPMG spectrum of *Sr$_3$(PO$_4$)$_2$ (19.8 T). Figure S13: ^{87}Sr NMR spectra of SrS and SrB$_6$. Figure S14: QUADFIT simulation of the MAS spectrum of SrB$_6$. Figure S15: QUADFIT simulation of the static spectrum of SrB$_6$. Figure S16: Experimental C_Q values (in MHz) vs GIPAW (PWSCF) and GIPAW (CA-STEP) data. Figure S17: Simulation of the static DFS−WURST−QCPMG spectrum of α-SrP$_2$O$_6$ (19.8 T). Figure S18: Comparison of the bond angle distributions around Ca and Sr, in the SiO$_2$−SrO and SiO$_2$−CaO−SrO glass models. Figure S19: Simulations (pure quadrupole lineshapes) of the ^{87}Sr sites in the five glass models of composition 76.9SiO$_2$−17.6CaO−5.5SrO and 93.4SiO$_2$−6.6SrO, for the different coordination numbers (CN) of Sr. Figure S20: Quadrupole analysis for strontium nuclei present in the glass models. Figure S21: ^{31}P and ^{1}H NMR characterization of B75-*Sr10 after immersion in SBF. Figure S22: μ-PIXE characterization of the glass grains after immersion in SBF (7 days). Table S1: Glass compositions, densities and cell information for the glass models. Table S2: Experimental and calculated (CASTEP) GIPAW ^{87}Sr NMR data for Sr derivatives. Table S3: Q^n distributions, Sr coordination and ^{29}Si NMR data for the 45S5−SrO glass model. Table S4: C_Q and η_Q parameters for ^{87}Sr in the glass models. This material is available free of charge via the Internet at http://pubs.acs.org.

■ AUTHOR INFORMATION

Corresponding Author
christian.bonhomme@upmc.fr

Notes
The authors declare no competing financial interest.

■ ACKNOWLEDGMENTS

■ REFERENCES

(1) Schroeder, H. A.; Titpton, I. H.; Nason, A. P. J. Chronic Dis. 1972, 25, 491.

(2) Zamburlini, M.; Campbell, J. L.; de Silveira, G.; Butler, R.; Pejovic-Milic, A.; Chettle, D. R. X-Ray Spectrom. 2009, 38, 271.

(3) Buelher, J.; Chappuis, P.; Saffar, J. L.; Tsouderos, Y.; Vignery, A. Bone 2001, 29, 176.

(4) Grynpas, M. D.; Hamilton, E.; Cheung, R.; Tsouderos, Y.; Deloffre, P.; Hott, M.; Marie, P. J. Bone 1996, 18, 253.

(5) Meunier, P. J.; Roux, C.; Seeman, E.; Ortolani, S.; Badurski, J. E.; Spector, T. D.; Cannata, J.; Balogh, A.; Lemmel, E. M.; Pors-Nielsen, S.; Rizzoli, R.; Genant, H. K.; Reginster, J. Y. New Engl. J. Med. 2004, 350, 459.

(6) Reginster, J. Y.; Seeman, E.; De Vernejoul, M. C.; Adami, S.; Compston, J.; Phenekos, C.; Devogelaer, J. P.; Curiel, M. D.; Sawicki, A.; Goemaere, S.; Sorensen, O. H.; Felsenberg, D.; Meunier, P. J. J. Clin. Endocrinol. Metab. 2005, 90, 2816.

(7) Isaac, J.; Nohra, J.; Lao, J.; Jallot, E.; Nedelec, J. M.; Berdal, A.; Sautier, J. M. Eur. Cells Mater. 2011, 21, 130.

(8) Zhang, W.; Shen, Y.; Pan, H.; Lin, K.; Liu, X.; Darvell, B. W.; Lu, W. W.; Chang, J.; Deng, L.; Wang, D.; Huang, W. Acta Biomater. 2011, 7, 800.

(9) Hesaraki, S.; Gholami, M.; Vazherad, S.; Shahrabi, S. Mater. Sci. Eng. 2010, C 30, 383.

(10) Raffalt, A. C.; Andersen, J. E. T.; Christgau, S. Anal. Bioanal. Chem. 2008, 391, 2199.

(11) Jallot, E.; Lao, J.; Nedelec, J.-M.; Sautier, J.-M.; Isaac, J. Strontium doped bioactive glasses. US Patent 2010/0278902 A1, Nov 4, 2010.

(12) Hill, R. G.; Stevens, M. M. Bioactive glass. US Patent, US 2009/0208428 A1; 2009.

(13) Lao, J.; Jallot, E.; Nedelec, J. M. Chem. Mater. 2008, 20, 4969.

(14) Lao, J.; Nedelec, J. M.; Jallot, E. J. Mater. Chem. 2009, 19, 2940.

(15) O'Donnell, M. D.; Hill, R. G. Acta Biomater. 2010, 6, 2382.

(16) Oudadesse, H.; Dietrich, E.; Bui, X. V.; Le Gal, Y.; Pellen, P.; Cathelineau, G. Appl. Surf. Sci. 2011, 257, 8587.

(17) Fredholm, Y. C.; Karpukhina, N.; Law, R. V.; Hill, R. G. J. Non-Cryst. Solids 2010, 356, 2546.

(18) Gorustovich, A. A.; Steimetz, T.; Cabrini, R. L.; Porto López, J. M. J. Biomed. Mater. Res., Part A 2010, 92A, 232.

(19) Taherkani, S.; Moztarzadeh, F.; Mozafari, M.; Lotfibakhshaiesh, N. J. Non-Cryst. Solids 2012, 358, 342.

(20) Goel, A.; Rajagopal, R. R.; Ferreira, J. M. F. Acta Biomater. 2011, 7, 4071.

(21) Galiano, P. G.; Porto Lopez, J. M.; Varetti, E. L.; Sobrados, I.; Sanz, J. Mater. Res. Bull. 1994, 29, 1297.

(22) Fujikura, K.; Karpukhina, N.; Kasuga, T.; Brauer, D. S.; Hill, R. G.; Law, R. V. J. Mater. Chem. 2012, 22, 7395.

(23) Xiang, Y.; Du, J. Chem. Mater. 2011, 23, 2703.

(24) Dorozhkin. J. Mater. Sci. 2007, 42, 1061.

(25) Dahl, S. G.; Allain, P.; Marie, P. J.; Mauras, Y.; Boivin, G.; Ammann, P.; Tsouderos, Y.; Delmas, P. D.; Christiansen, C. Bone 2001, 28, 446.

(26) Bradley, D. A.; Muthuvelu, P.; Ellis, R. E.; Green, E. M.; Attenburrow, D.; Barrett, R.; Arkill, K.; Colridge, D. B.; Winlove, C. P. Nucl. Instrum. Methods Phys. Res. B 2007, 263, 1.

(27) Stahl, K.; Andersen, J. E. T.; Christgau, S. Acta Crystallogr., Sect. C: Cryst. Struct. Commun., 2006, C62, m144.

(28) Allison, N.; Finch, A. A.; Newville, M.; Sutton, S. R. Geochim. Cosmochim. Acta 2005, 69, 3801.

(29) Mear, F. O.; Yot, P. G.; Kolobov, A. V.; Ribes, M.; Guimon, M. F.; Gonbeau, D. J. Non-Cryst. Solids 2007, 353, 4640.

(30) Berry, F. J.; Marco, J. F.; Ren, X. J. Solid State Chem. 2005, 178, 961.

(31) Finch, A. A.; Allison, N.; Sutton, S. R.; Newville, M. Geochim. Cosmochim. Acta 2003, 67, 1189.

(32) O'Day, P. A.; Newville, M.; Neuhoff, P. S.; Sahaia, N.; Carroll., S. A. J. Colloid Interface Sci. 2000, 222, 184.

(33) Bazin, D.; Rehr, J. J.; Thiaudière, D.; Reguer, S. *J. Synchr. Radiat.* **2011**, *18*, 912.

(34) Larsen, F. H.; Skibsted, J.; Jakobsen, H. J.; Nielsen, N. C. *J. Am. Chem. Soc.* **2000**, *122*, 7080.

(35) Ishida, K.; Minami, Y.; Kitaoka, Y.; Nakatsuji, S.; Kikugawa, N.; Maeno, Y. *Phys. Rev. B* **2003**, *67*, 214412.

(36) Gervais, C.; Veautier, D.; Smith, M. E.; Babonneau, F.; Belleville, P.; Sanchez, C. *Solid State Nucl. Magn. Reson.* **2004**, *26*, 147.

(37) Bowers, G. M.; Mueller, K. T. *Phys. Rev. B* **2005**, *71*, 224112-1−7.

(38) Bowers, G. M.; Ravella, R.; Komarneni, S.; Mueller, K. T. *J. Phys. Chem. B* **2006**, *110*, 7159.

(39) Bowers, G. M.; Lipton, A. S.; Mueller, K. T. *Solid State Nucl. Magn. Reson.* **2006**, *29*, 95.

(40) (a) MacKenzie, K. J. D.; Smith, M. E. *Multinuclear Solid State NMR of Inorganic Materials*; Pergamon Materials Series, Pergamon: New York, 2002. (b) Smith, M. E.; van Eck, E. R. H. *Prog. Nucl. Magn. Reson. Spectrosc.* **1999**, *34*, 159.

(41) Siegel, R.; Nakashima, T. T.; Wasylichen, R. E. *Concepts Magn. Reson., Part A* **2005**, *26A*, 62.

(42) Iuga, D.; Schäfer, H.; Verhagen, R.; Kentgens, A. P. M. *J. Magn. Reson.* **2000**, *147*, 192.

(43) O'Dell, L. A.; Schurko, R. W. *Chem. Phys. Lett.* **2008**, *464*, 97.

(44) O'Dell, L. A.; Rossini, A. J.; Schurko, R. W. *Chem. Phys. Lett.* **2009**, *468*, 330.

(45) Jakobsen, H. J.; Bildsoe, H.; Skibsted, J.; Brorson, M.; Srinivasan, B. R.; Naether, C.; Bensch, W. *Phys. Chem. Chem. Phys.* **2009**, *11*, 6981.

(46) Lucier, B. E. G.; Tang, J. A.; Schurko, R. W.; Bowmaker, G. A.; Healy, P. C.; Hanna, J. V. *J. Phys. Chem. C* **2010**, *114*, 7949.

(47) MacGregor, A. W.; O'Dell, L. A.; Schurko, R. W. *J. Magn. Reson.* **2011**, *208*, 103.

(48) O'Dell, L. A.; Schurko, R. W.; Harris, K. J.; Autschbach, J.; Ratcliffe, C. I. *J. Am. Chem. Soc.* **2011**, *133*, 527.

(49) Pickard, C. J.; Mauri, F. *Phys. Rev. B* **2001**, *63*, 245101-1−13.

(50) Charpentier, T. *Solid State Nucl. Magn. Reson.* **2011**, *40*, 1 (and references therein).

(51) The "B75-Sr10" name was chosen to simplify the name of the sample: "B" is for "bioactive glass", "75" and "10" for the respective Si and Sr wt % targeted in the synthesis.

(52) Reinholdt, M.; Croissant, J.; di Carlo, L.; Granier, D.; Gaveau, P.; Bégu, S.; Devoisselle, J. M.; Mutin, H.; Smith, M. E.; Bonhomme, C.; Gervais, C.; van der Lee, A.; Laurencin, D. *Inorg. Chem.* **2011**, *50*, 7802.

(53) Höppe, H. A. *Solid State Sci.* **2005**, *7*, 1209.

(54) Soulie, J.; Nedelec, J. M.; Jallot, E. *Phys. Chem. Chem. Phys.* **2009**, *11*, 10473.

(55) Kokubo, T.; Takadama, H. *Biomaterials* **2006**, *27*, 2907.

(56) Bohner, M.; Lemaître, J. *Biomaterials* **2009**, *30*, 2175.

(57) Jones, J. R.; Sepulveda, P.; Hench, L. L. *J. Biomed. Mater. Res.* **2001**, *58*, 720.

(58) Pedone, A.; Charpentier, T.; Menziani, M. C. *Phys. Chem. Chem. Phys.* **2010**, *12*, 6054.

(59) Zhang, P.; Grandinetti, P. J.; Stebbins, J. F. *J. Phys. Chem. B* **1997**, *101*, 4004.

(60) Hung, I.; Gan, Z. *J. Magn. Reson.* **2010**, *204*, 256.

(61) Pauvert, O.; Fayon, F.; Rakhmatullin, A.; Krämer, S.; Horvatić, M.; Avignant, D.; Berthier, C.; Deschamps, M.; Massiot, D.; Bessada, C. *Inorg. Chem.* **2009**, *48*, 8709.

(62) Massiot, D.; Farnan, I.; Gautier, N.; Trumeau, D.; Trokiner, A.; Coutures, J.-P. *Solid State Nucl. Magn. Reson.* **1995**, *4*, 241.

(63) Fayon, F.; Landron, C.; Sakurai, K.; Bessada, C.; Massiot, D. *J. Non-Cryst. Solids* **1999**, *243*, 39.

(64) Rossini, A. J.; Mills, R. W.; Briscoe, G. A.; Norton, E. L.; Geier, S. J.; Hung, I.; Zheng, S.; Autschbach, J.; Schurko, R. W. *J. Am. Chem. Soc.* **2009**, *131*, 3317.

(65) Massiot, D.; Fayon, F.; Capron, M.; King, I.; Le Calvé, S.; Alonso, B.; Durand, J. O.; Bujoli, B.; Gan, Z.; Hoatson, G. *Magn. Reson. Chem.* **2002**, *20*, 70. See also: http://www.cemhti.cnrs-orleans.fr/.

(66) Kemp, T. F.; Smith, M. E *Solid State Nucl. Magn. Reson.* **2009**, *35*, 243.

(67) (a) Hench, L. L.; Splinter, R. J.; Alen, W. C.; Greelee, T. K. *J. Biomed. Mater. Res.* **1971**, *2*, 117. (b) Hench, L. L.; Polak, J. M. *Science* **2002**, *295* (1014), 1016−1017. (c) Hench, L. L. *J. Mater. Sci. Mater. Med.* **2006**, *17*, 967.

(68) Du, J.; Xiang, Y. *J. Non-Cryst. Solids* **2012**, *358*, 1059.

(69) Du, J.; Cormack, A. N. *J. Am. Ceram. Soc.* **2005**, *88*, 2532.

(70) Du, J.; Corrales, L. R. *J. Non-Cryst. Solids* **2006**, *352*, 3255.

(71) Smith, W.; Forester, T. *J. Mol. Graphics* **1996**, *14*, 136.

(72) Kresse, G.; Hafner, J. *Phys. Rev. B* **1993**, *47*, 558.

(73) Kresse, G.; Hafner, J. *Phys. Rev. B* **1994**, *49*, 14251.

(74) Blöchl, P. E. *Phys. Rev. B* **1994**, *50*, 17953.

(75) Kresse, G.; Joubert, D. *Phys. Rev. B* **1999**, *59*, 1758.

(76) Perdew, J. P.; Burke, K.; Ernzerhof, M. *Phys. Rev. Lett.* **1996**, *77*, 3865.

(77) Perdew, J. P.; Burke, K.; Ernzerhof, M. *Phys. Rev. Lett.* **1997**, *78*, 1396.

(78) Monkhorst, H. J.; Pack, J. D. *Phys. Rev. B* **1976**, *13*, 5188.

(79) Giannozzi, P.; Baroni, S.; Bonini, N.; Calandra, M.; Car, R.; Cavazzoni, C.; Ceresoli, D.; Chiarotti, G. L.; Cococcioni, M.; Dabo, I.; Dal Corso, A.; de Gironcoli, S.; Fabris, S.; Fratesi, G.; Gebauer, R.; Gerstmann, U.; Gougoussis, C.; Kokalj, A.; Lazzeri, M.; Martin-Samos, L.; Marzari, N.; Mauri, F.; Mazzarello, R.; Paolini, S.; Pasquarello, A.; Paulatto, L.; Sbraccia, C.; Scandolo, S.; Sclauzero, G.; Seitsonen, A. P.; Smogunov, A.; Umari, P.; Wentzcovitch, R. M. *J. Phys. Condens. Matter* **2009**, *21*, 395502-1−19.

(80) Troulier, N.; Martins, J. L. *Phys. Rev. B* **1991**, *43*, 1993.

(81) Rappe, A. M.; Rabe, K. M.; Kaxiras, E.; Joannopoulos, J. D. *Phys. Rev. B* **1990**, *41*, 13175.

(82) Kleinman, L.; Bylander, D. *Phys. Rev. Lett.* **1982**, *48*, 1425.

(83) Laasonen, K.; Pasquarello, A.; Car, R.; Lee, C.; Vanderbilt, D. *Phys. Rev. B* **1993**, *47*, 10142.

(84) Clark, S. J.; Segall, M. D.; Pickard, C. J.; Hasnip, P. J.; Probert, M. J.; Refson, K.; Payne, M. C. *Z. Kristallogr.* **2005**, *220*, 567.

(85) Pyykko, P. *Mol. Phys.* **2008**, *106*, 1965.

(86) (a) Laurencin, D.; Gervais, C.; Wong, A.; Coelho, C.; Mauri, F.; Massiot, D.; Smith, M. E.; Bonhomme, C. *J. Am. Chem. Soc.* **2009**, *131*, 13430. (b) Laurencin, D.; Wong, A.; Hanna, J. V.; Dupree, R.; Smith, M. E. *J. Am. Chem. Soc.* **2008**, *130*, 2412. (c) Laurencin, D.; Smith, M. E. *Prog. Nucl. Magn. Reson. Spectrosc.* **2012**, DOI: 10.1016/j.pnmrs.2012.05.001.

(87) Hamaed, H.; Laschuk, M. W.; Terskikh, V. V.; Schurko, R. W. *J. Am. Chem. Soc.* **2009**, *131*, 8271.

(88) As further confirmation of this, it should be noted that in the case of a phase pure nonlabeled $SrHPO_4$ sample, no significant signal was obtained after 12 h of acquisition on a 600 MHz NMR magnet, despite the use of low power ^1H CW decoupling.

(89) Charpentier, T.; Kroll, P.; Mauri, F. *J. Phys. Chem. C* **2009**, *113*, 7917−7929.

(90) Angeli, F.; Villain, O.; Schuller, S.; Ispas, S.; Charpentier, T. *Geochim. Cosmochim. Acta* **2011**, *75*, 2453−2469.

(91) Pedone, A.; Charpentier, T.; Menziani, M. C. *J. Mater. Chem.* **2012**, *22*, 12599.

(92) It should be noted that just like ^{87}Sr, ^{29}Si NMR values are properly reproduced by GIPAW. For example, concerning $SrSiO_3$ (Q^2 units), the unique experimental chemical shift corresponds to $\delta_{iso}(^{29}Si)$ = −84.7 ppm (Figure S10), while GIPAW calculations predict two very closely isotropic chemical shifts ($\delta_{iso}(^{29}Si)$ = −83.9 and −84.0 ppm, footnote in Table 1).

(93) NMR parameters were calculated using GIPAW for all five of the glass models in the SiO_2−CaO−SrO and SiO_2−SrO phase diagrams, but for only one of five of the glass models of SiO_2−Na_2O−CaO−SrO−P_2O_5 (as this model is chemically different from the B75-Sr10 phase).

(94) Pedone, A.; Charpentier, T.; Malavasi, G.; Menziani, M. C. *Chem. Mater.* **2010**, *22*, 5644.

(95) It should be noted that because of the limited number of sites, the calculated ^{29}Si NMR data could have been smoothed to ensure a

better comparison with the experimental spectrum in Figure 4, either by applying a Gaussian convolution in the frequency domain or by applying a kernel density estimation (KDE) procedure directly on the NMR chemical shift distribution (see ref 58). However, this is beyond the scope of this contribution.

(96) Unfortunately, for each new model developed for Sr-substituted glasses, the computational cost is very high (MD, DFT, and the GIPAW calculations), which explains why only five models of each composition were studied here.

(97) Ghose, S.; Tsang, T. *Am. Mineral.* **1973**, *58*, 748.

(98) Park, B.; Corrales, L. R. *J. Non-Cryst. Solids* **2002**, *311*, 107.

(99) (a) Brawer, S. A.; Weber, M. J. *J. Non-Cryst. Solids* **1980**, *38 & 39*, 9. (b) Weber, M. J.; Brewer, S. A. *J. Non-Cryst. Solids* **1982**, *52*, 321.

(100) Du, J.; Cormack, A. N. *J. Non-Cryst. Solids* **2005**, *351*, 2263−2276.

(101) It should be noted that for other alkaline-earth nuclei such as ^{25}Mg and ^{43}Ca, clear relationships between the quadrupolar coupling constant C_Q and simple geometrical factors are also difficult to establish (see ref 86 for example).

(102) The chemical analyses of the bioactive glass powders before and after immersion show that ∼80% of the initial Sr content are released in the SBF medium. It follows that the number of ^{87}Sr spins is divided by ∼5 after immersion. To obtain the same signal-to-noise ratio, the initial experimental time (B75-*Sr10 *before* immersion, 1 h in Figure 7) has to be multiplied by 25. In Figure 7, it is clear that a comparable signal-to-noise ratio has not been reached after 16 h (for B75-*Sr10 *after* immersion).

(103) Jäger, C.; Welzel, T.; Meyer-Zaika, W.; Epple, M. *Magn. Reson. Chem.* **2006**, *44*, 573−580.

(104) It should be noted that the ^{1}H and ^{31}P NMR analyses were carried out ∼1 month after removal of the glasses from SBF. Only HAp was detected at the time of the measurement, while no distinct trace of an octacalcium phosphate phase was observed.

(105) It should be noted that previous *μ*-PIXE imaging of the mineralized layer at the surface of Sr-doped glasses in contact with DMEM (a common cell culture medium) had also demonstrated the incorporation of Sr ions into the newly formed calcium phosphate surface layer (see ref 13).

(106) Davis, M. C.; Brouwer, W. J.; Wesolowski, D. J.; Anovitz, L. M.; Lipton, A. S.; Mueller, K. T. *Phys. Chem. Chem. Phys.* **2009**, *11*, 7013.

(107) (a) Ohta, H.; Sugiura, K.; Koumoto, K. *Inorg. Chem.* **2008**, *471*, 8429−8436. (b) Ohta, H. *Mater. Today* **2007**, *10*, 44−49. (c) Haeni, J. H.; Irvin, P.; Chang, W.; Uecker, R.; Reiche, P.; Li, Y. L.; Choudhury, S.; Tian, W.; Hawley, M. E.; Craigo, B.; Tagantsev, A. K.; Pan, X. Q.; Streiffer, S. K.; Chen, L. Q.; Kirchoefer, S. W.; Levy, J.; Schlom, D. G. *Nature* **2004**, *430*, 758−761. (d) Alkoy, S.; Duran, C.; Hall, D. A. *J. Am. Ceram. Soc.* **2008**, *91*, 1597−1602. (e) Hardy, A.; Van Elshocht, S.; Adelmann, C.; Kittl, J. A.; De Gendt, S.; Heyns, M.; D'Haen, J.; D'Olieslaeger, M.; Van Bael, M. K.; Van den Rul, H.; Mullensa., J. *Acta Mater.* **2010**, *58*, 216−225. (f) Maneo, Y.; Hashimoto, H.; Yoshida, K.; Nishisaki, S.; Fujita, T.; Bednorz, J. D.; Lichtenberg, F. *Nature* **1994**, *372*, 532−534.